JOURNAL OF GEOPHYSICAL RESEARCH, VOL. 112, C09024, doi:10.1029/2006JC003881, 2007

Turbulence intensity in the wave boundary layer and bottom friction under (mainly) flat bed conditions

John P. Newgard[1] and Alex E. Hay[1]

Received 14 August 2006; revised 5 February 2007; accepted 11 June 2007; published 27 September 2007.

[1] Variations with wave energy of near-bed turbulence and the wave friction factor are investigated in the near-shore zone for bed states spanning low-steepness sand ripples and flat bed, and for wave energies extending well into the sheet flow regime. The measurements were made using a 1.7-MHz pulse-coherent Doppler profiler in ca. 3-m mean water depth. Near-bed turbulence intensities, phase-averaged over the highest-1/3 waves, peak at phases between 10° and 55° after the wave crest, this phase decreasing with increasing wave Reynolds number. Wave friction factors computed from near-bed vertical turbulence intensity fall within the range predicted by existing semi-empirical formulae, and exhibit broadly similar trends. At the higher end of the observed wave energy range (i.e., in the sheet flow regime), however, the measured friction factors increase with sea-and-swell energy faster than the predictions. This anomalous increase is correlated with infragravity wave energy and with mean cross-shore current speed, but not with other forcing parameters including mean long-shore current speed, wave skewness, wave asymmetry and wave breaking frequency. It is argued that the anomaly is partly due to additional near-bed turbulence associated with infragravity waves, and therefore that these data are not inconsistent with Wilson's (1989) parameterization for bottom roughness in oscillatory sheet flow. Peak near-bed turbulence intensities are independent of wave Reynolds number for $Re \lesssim 1.2 \times 10^6$, but proportional to Re for $Re \gtrsim 1.2 \times 10^6$, this abrupt change possibly indicating a critical dependence on Re of turbulence production in the WBL over flat or nearly flat mobile beds.

Citation: Newgard, J. P., and A. E. Hay (2007), Turbulence intensity in the wave boundary layer and bottom friction under (mainly) flat bed conditions, *J. Geophys. Res.*, *112*, C09024, doi:10.1029/2006JC003881.

1. Introduction

[2] The vertical turbulent flux of momentum from surface gravity waves to the seabed is a primary forcing mechanism for the suspension and transport of seafloor sediments on the continental shelf and in the near-shore zone. Recent work has also shown that bottom friction is a significant energy dissipation mechanism for waves propagating across sandy continental shelves [*Young and Gorman*, 1995; *Ardhuin et al.*, 2003]. Considerable uncertainty exists, however, in the parameterization of bottom friction for beds of mobile sediment at a given wave-forcing condition [see for example, *Tolman*, 1994]. The uncertainty is due in part to the complications of seabed adjustment among a range of possible bed states [*Hay and Mudge*, 2005], and in part to the fact that the parameterizations are based mainly on laboratory experiments and have until recently remained largely untested in the field.

[3] In particular, for the high wave energy conditions corresponding to sheet flow, the relation for the effective bed roughness suggested by *Wilson* [1989] is based on laboratory measurements in unidirectional flow. Wilson argued that the unidirectional result could be extended to oscillatory flow, and *Tolman* [1994] used the Wilson relation for sheet flow roughness in his formulation of the wave boundary layer equations. However, the fact that this relation is based on unidirectional flow measurements led Tolman to remark that "the choice of sheet-flow roughness model presently remains somewhat arbitrary." Thus a question exists as to how well the Wilson formula performs for wave-driven sheet flow in natural wave conditions. This paper represents an attempt to address that question.

[4] Thus a central goal of the paper is to determine the bottom drag coefficient for wind waves over a sandy seafloor in the high-energy sheet flow regime, in order to test the validity of the *Wilson* [1989] relation for sheet flow roughness. In the field, waves are usually irregular (i.e., of variable height and period), and are typically characterized by the "significant wave": i.e., the average of the highest-1/3 waves in the wave height distribution. The bottom drag coefficient for waves is based on the maximum shear stress during a wave cycle. A question then arises, for irregular waves, as to whether the drag coefficient based on the average turbulence intensity and the significant wave orbital velocity is the same as or different from the drag coefficient determined from the average of the maximum stress and the orbital velocity amplitude for the highest-1/3 waves. Con-

[1]Department of Oceanography, Dalhousie University, Halifax, Nova Scotia, Canada.

0148-0227/07/2006JC003881$09.00

sequently, one of the secondary objectives of the paper is to compare the results from these two different methods for estimating the bottom drag coefficient for the highest-1/3 waves.

[5] A second goal is to investigate the properties of near-bed turbulence above mobile beds at high values of the Shields parameter. Several questions relating directly to turbulence are pursued as an integral part of the analysis. The ensemble-averaged turbulence intensity as a function of wave phase is obtained as a by-product of determining the maximum stress and orbital velocity amplitude for individual waves. This dependence of near-bed turbulence intensity on wave phase, in addition to providing one of the main bases of comparison between the present field measurements and previous results from laboratory and numerical experiments, is used to investigate the influence of wave Reynolds number on turbulence intensity. In addition, the vertical structure of the phase-averaged turbulence is used to shed light on the likely contribution from wave breaking to near-bed turbulence in the present data set.

[6] The paper is organized as follows. Section 2 briefly outlines wave bottom boundary layer (WBL) theory and the relevant relations for the wave friction factor. In section 3, the experiment site and instrumentation are summarized, and the data analysis procedures described. Also, because we are interested here mainly in wave-driven flat bed conditions, data runs corresponding most closely to these conditions were chosen. The selection criteria are described in section 3. The results are presented in section 4, in the following order: bed roughness, Shields parameter and other forcing parameter statistics, near-bed turbulence intensities, the probability distribution function for the RMS vertical turbulent velocity, the wave friction factor estimates, wave orbital velocity amplitude distributions, wave breaking frequencies, and other sources of near-bed turbulent kinetic energy. In section 4, the data are partitioned into four Intervals of increasing Shields parameter (roughly equivalent to wave energy here), to elucidate the relationships among near-bed turbulence intensity, the wave friction factor, and forcing parameter statistics as a function of wave energy. In the Discussion, section 5, the method for extrapolating the turbulence spectrum into the wind-wave band is examined, and the relative importance of turbulence from infragravity waves and mean currents is assessed. In addition, an approximate correction to the sea-and-swell wave friction factor estimates for the effects of infragravity wave energy is determined, yielding an estimate of the bottom drag coefficient for infragravity waves from the turbulence data. The main results and conclusions of the paper are summarized in section 6.

2. Theory

[7] The theory for the turbulent wave bottom boundary layer has been treated in detail elsewhere [e.g., *Fredsoe and Deigaard*, 1992]. Briefly summarizing, the linearized momentum equation in the boundary layer can be written in the form

$$\rho \frac{\partial}{\partial t}(\tilde{u} - \tilde{u}_\infty) = \frac{\partial \tau}{\partial z}, \tag{1}$$

where $\tilde{u} = \tilde{u}(\vec{x}, z, t)$ is the wave orbital velocity within the boundary layer, ρ is the fluid density, τ is the shear stress, $\vec{x}$ is the horizontal coordinate (aligned with the direction of wave propagation), z is the vertical coordinate (positive upward), and t is time. The usual boundary layer approximation has been invoked to obtain equation (1): that is, horizontal scales are assumed to be much greater than vertical scales, allowing the horizontal pressure gradient in the boundary layer to be replaced by the acceleration of the flow in the interior. The latter is assumed to be sinusoidal: i.e., $\tilde{u}_\infty(t) = \tilde{u}_o \cos \omega t$ at $x = 0$, $\tilde{u}_o$ being the wave orbital velocity amplitude, $\omega = 2\pi/T$ the angular frequency, and T the wave period. As will be seen, the waves in this study were non-linear as well as irregular. It is well known that linear wave theory holds to a very good approximation locally in the near-shore, both within and outside the surf zone [*Guza and Thornton*, 1980]. Thus equation (1) is expected to apply to each constituent frequency in the wave spectrum even under non-linear waves, and therefore also to the linear sum over the locally measured spectral constituents of the wavefield. The contributions from non-linear advection terms to the momentum balance have been neglected in equation (1). These terms are $O(\tilde{u}_o/c)$ [*Schlichting*, 1932; see also *Schlichting*, 1979, p. 428, and *Trowbridge and Madsen*, 1984], where c is the phase velocity of the waves. The highest value of the significant wave orbital velocity and ca. 9-s significant wave periods in the present study yield $\tilde{u}_o/c \sim 0.2$. Thus $\tilde{u}_o/c$ is typically much less than unity for the results to be presented, justifying our use of the linearized boundary layer equations.

[8] Assuming a time-independent eddy viscosity of the form $\nu_e = \kappa u_* z$, equation (1) can be solved analytically. With τ_0, the maximum stress during the wave cycle, expressed as

$$\tau_0 = \frac{1}{2}\rho f_w \tilde{u}_o^2 \tag{2}$$

where f_w is the wave friction factor [*Jonsson*, 1966, 1980], and assuming no slip at the bed, the resulting solution yields expressions for the friction factor

$$f_w = 2\kappa^2 \zeta_o \frac{\mathrm{ker}_1^2 2\sqrt{\zeta_o} + \mathrm{kei}_1^2 2\sqrt{\zeta_o}}{\mathrm{ker}^2 2\sqrt{\zeta_o} + \mathrm{kei}^2 2\sqrt{\zeta_o}}, \tag{3}$$

and the relative roughness

$$\frac{k_N}{2A} = 21.2\kappa\sqrt{f_w}\zeta_o, \tag{4}$$

where $\kappa = 0.4$ is the von Karman constant, ker and kei are Kelvin functions, k_N is the Nikuradse equivalent roughness of the bed, A is the wave orbital semi-excursion, $\zeta_o = \omega z_o/\kappa u_*$, and the flow is rough turbulent ($z_0 = k_N/30$).

[9] For beds of mobile cohesionless sediment, k_N includes contributions from ripples (when present) and from the moving sediment grains. *Grant and Madsen* [1982] expressed the total roughness as the algebraic sum of a component due to ripple form drag and a component due to sediment transport. Thus writing $k_N = k_r + k_{sf}$, *Tolman*

[1994] combined the roughness predictor suggested by *Madsen et al.* [1990] for ripples formed under irregular waves,

$$k_r = 1.5A\left(\frac{\theta_d}{\theta_c}\right)^{-2.5}, \tag{5}$$

with the sheet flow parameterization introduced by *Wilson* [1989],

$$k_{sf} = 0.0655A\left(\frac{\tilde{u}_{1/3}^2}{(s-1)gA}\right)^{1.4}. \tag{6}$$

In these relations, s is the specific gravity of the sediment grains, g the gravitational acceleration, $\tilde{u}_{1/3}$ the significant wave orbital velocity, θ_d the grain roughness Shields parameter (see below), and $\theta_c \simeq 0.05$ the critical Shields parameter for sediment motion. Note that equation (6) is based on unidirectional flow measurements, extended by Wilson to the oscillatory flow case.

[10] For mobile bed roughness due solely to skin friction (i.e., no ripples and no sheet flow), the wave friction factor is denoted by f_w' to be consistent with the notation used by *Tolman* [1994]. For fixed grains on a flat bed, an empirical expression for f_w' based on laboratory experiments with regular waves is [*Swart*, 1974; see also *Nielsen*, 1992].

$$f_w' = \exp\left[5.213\left(\frac{r}{A}\right)^{0.194} - 5.977\right], \tag{7}$$

where r is the bed roughness. In this paper, the value of r in equation (7) is set equal either to the median grain diameter, d_{50}, or to 2.5 d_{50} [*Nielsen*, 1992, p. 105], and the corresponding f_w' values are denoted by f_w' or $f_{2.5}'$ respectively. The flat bed friction factor for non-sheet flow conditions can also be computed using equations (3) and (4), with k_N replaced by a representative grain roughness. The results of such computations, with $k_N = d_{50}$ or 2.5 d_{50}, are included here for comparison to equation (7).

[11] The Shields parameter is given by [see for example *Nielsen*, 1992, p. 104]

$$\theta = \frac{f_w\tilde{u}_o^2/2}{(s-1)gd_{50}}. \tag{8}$$

With f_w in equation (8) replaced by f_d' or $f_{2.5}'$, the grain roughness Shields parameter is denoted by θ_d or $\theta_{2.5}$ respectively.

[12] The maximum bed shear stress can be expressed as

$$\tau_0 = \rho u_*^2, \tag{9}$$

where u_* is the friction velocity. Laboratory observations have indicated that u_* can be estimated from near-bed vertical turbulent velocity fluctuations [*van Doorn*, 1981; see also *Nielsen*, 1992, p. 72; *Sleath*, 1987; and *Jensen et al.*, 1989]:

$$u_* = 2w_{rms}', \tag{10}$$

where w_{rms}' is the RMS vertical turbulent velocity. Thus, combining equation (10) with equations (2) and (9), measurements of w_{rms}' can be used to estimate the wave friction factor. Given the $O(10)$-cm thickness of the WBL, this approach is appealing from the standpoint of field measurements, since acoustic Doppler techniques can be used to remotely measure the vertical turbulent velocity just above the bed without disturbing the near-bed flow. The method was used by *Smyth and Hay* [2003], who obtained promising comparisons between predicted and observed friction factors as a function of bed state (i.e., three different ripple types, and flat bed). The approach is pursued here, but with a focus on high energy conditions when sheet flow is expected. For reasons which will be made clear later, we introduce a scaling factor Λ such that $u_* = 2\Lambda w_{rms}'$, and the relationship between f_w and w_{rms}' becomes

$$f_w = 2\left(\frac{2\Lambda w_{rms}'}{\tilde{u}_o}\right)^2. \tag{11}$$

3. The SandyDuck97 Experiment

3.1. Field Site

[13] The data were collected during the SandyDuck97 experiment at the U.S. Army Corps of Engineers Field Research Facility (FRF) from August 26 to November 8, 1997. The FRF, located on the Outer Banks of North Carolina, is described in *Birkemeier et al.* [1985]. The beach profile throughout most of the experiment was characterized by a well-defined near-shore bar and a smaller offshore bar, as illustrated in Figure 1. The data reported here are mainly from frame B, deployed between the two bars in approximately 3-m mean water depth. Some data from frame C, located 35 m seaward of frame B, are also discussed.

[14] Based on the cross-shore bathymetric profiles acquired with the FRF Coastal Research Amphibious Buggy (CRAB) along transects 30 m to the north and 20 m to the south of the instrument line, water depths at frame B ranged from 3.10 to 3.50 m (3.29 ± 0.06 m, mean ± standard deviation), and from 3.34 to 3.50 m at frame C (3.42 ± 0.03 m). Local bed slopes estimated from the average of the two profiles, within ± 5 m cross-shore distance of the instrument frame, ranged from 0.2° to 1.3° (0.8° mean). Grain size distributions, obtained by sieve analysis of 11 sediment samples collected within 20 m of frame B in the cross-shore direction and 300-m alongshore, yielded $d_{50} = 170 \pm 15$ μm, with $d_{16} = 133 \pm 92$ μm and $d_{84} = 236 \pm 32$ μm, where the subscripts denote cumulative percent finer. The median grain diameter at frame C was 145 μm, finer than that at B.

3.2. Instrumentation

[15] The instrument frame geometry is illustrated in Figure 2. The upper section of the frame was constructed from 3-cm diameter galvanized steel pipe, and clamped to four 7-m long, 6-cm diameter vertical steel pipes jetted approximately 5 m into the bed. The instruments were mounted on the end of a cantilevered mast, as illustrated in Figure 3. The sensors included a single-beam, 1.7 MHz pulse-coherent acoustic Doppler profiler (CDP), a 5 MHz Sontek acoustic Doppler velocimeter (ADV-O), and a

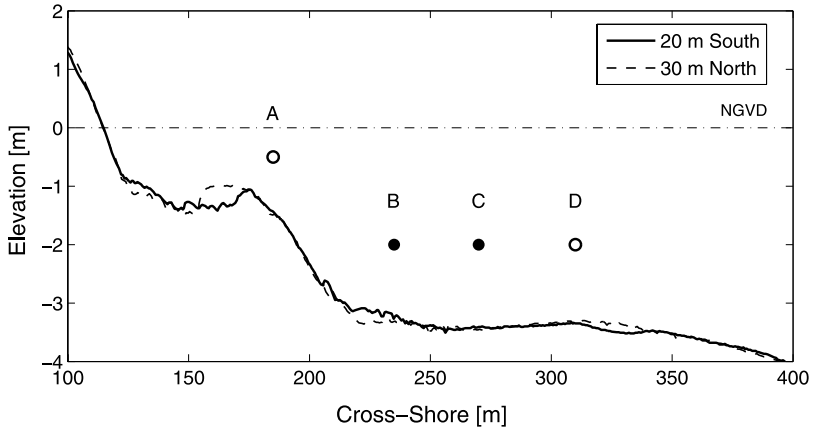

Figure 1. Cross-shore beach profiles measured with the CRAB along the two CRAB transects immediately to the north and south of the instrument line on Yearday 267 (September 24, 1997). The cross-shore distances are in the FRF coordinate system. The cross-shore locations of frames B and C are indicated. Elevations are relative to National Geodetic Vertical Datum (NGVD).

2.25 MHz Mesotech rotary pencil-beam sonar. The other instruments used in this study include 2.25 MHz Mesotech rotary pencil-beam and fan-beam sonars at frame C.

[16] Also illustrated in Figure 2 is the frame orientation relative to the FRF coordinate system. The instrument mast projected to the north and east away from the frame legs, so that the instruments would be upstream of the frame in the southward-flowing long-shore currents associated with Nor'easters, and also be minimally affected by the wakes and sediment plumes generated by the wave orbital flow past the instrument legs. The coordinate system used here is also shown in the figure: x is positive onshore, y positive alongshore toward the south, and z positive up. The corresponding velocity components are u, v, and w, with the same sign convention.

[17] The CDP measured vertical profiles of the vertical component of particle velocity with 0.7-cm vertical resolution. The data runs were approximately 20 min long, this time varying as the pulse-repetition rate was adjusted to accommodate changes in mean bed elevation. For the 89 data runs for which results are reported here, the average duration was 23.5 min, and the minimum 18 min. The runs were acquired half-hourly during storms and every second hour otherwise. The sampling rate of ensemble-averaged profiles (24 profiles per ensemble) was 16 to 25 Hz, depending on distance to the bed (which ranged from

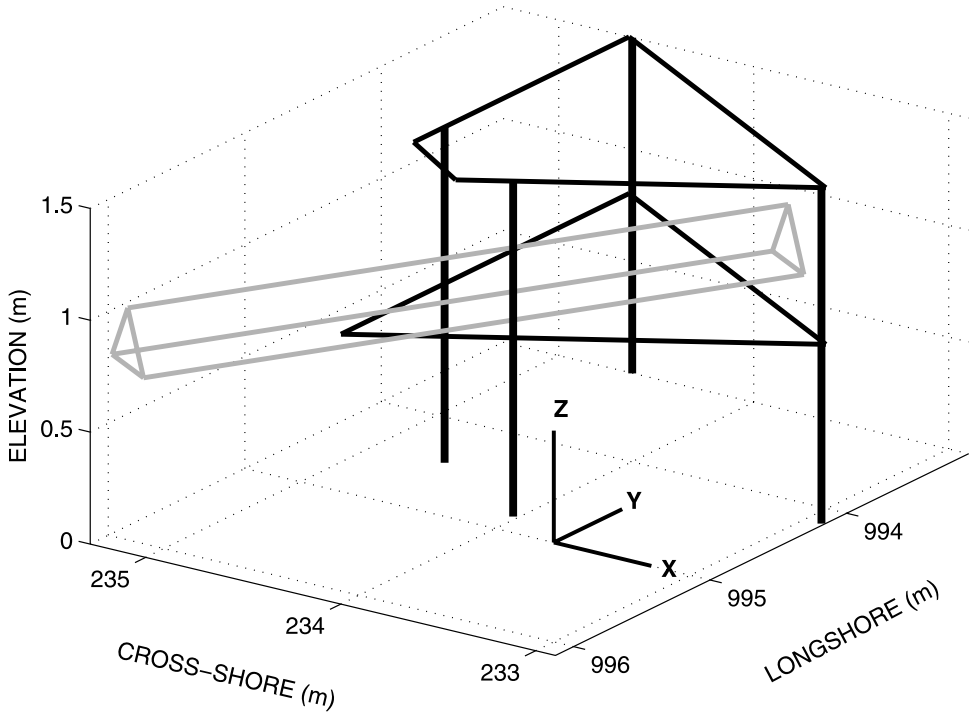

Figure 2. Schematic of the support frame (black) and cantilevered mast (grey) at frame B, showing the *xyz* coordinate system.

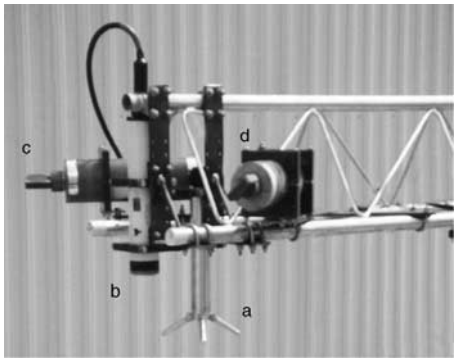

Figure 3. Photograph of instrumentation and the cantilevered mast that were deployed at frame B. Instruments include: (a) acoustic Doppler velocimeter (ADV); (b) coherent Doppler profiler (CDP); (c) upward-looking rotary pencil-beam sonar (not used in this study); (d) cross-shore rotary pencil-beam sonar.

0.75 to 1 m as bed elevation changed due to local erosion and accretion). With the 24-profile ensemble averaging, the accuracy of the velocity estimates is about 1 mm s^{-1}. Further details regarding the CDP system may be found in *Zedel and Hay* [1999].

[18] The ADV collected single-point estimates of 3 components of particle velocity at a sampling rate of 25 Hz. The elevation of the ADV sampling volume ranged from 45 to 75 cm as bed level changed during the experiment. The ADV was located approximately 15 cm shoreward of the CDP (Figure 3).

[19] The rotary fan-beam and pencil-beam sonars were used to determine bed state and bottom roughness. Five consecutive rotary sonar images were acquired every 10 minutes during storm conditions, and every half hour otherwise. Information regarding the fan-beam system, and on bed state variability during SandyDuck97, may be found in *Hay and Mudge* [2005].

3.3. Data Processing

[20] Wave orbital velocities in the sea-and-swell band, $\tilde{u}(t)$ and $\tilde{v}(t)$, were obtained by band-pass filtering the ADV velocity time series over the frequency range 0.05–0.5 Hz using a 5^{th}-order Butterworth filter. Wave phase, $\phi = \omega t$, was determined from the Hilbert transform of $\tilde{u}(t)$, with $\phi = 0$ at wave crests. Wave orbital velocity amplitude, $\tilde{u}_o$, was defined as half the peak-to-peak velocity during a wave cycle.

[21] To represent the time-averaged properties of irregular waves, the significant wave orbital velocity and semi-excursion, $\tilde{u}_{1/3}$ and $A_{1/3} = \tilde{u}_{1/3}/\omega$, are used in place of u_o and A in equations (2) to (8). In the results to be presented, $\omega = 2\pi/T_p$, where T_p is the peak period in the wind-wave energy spectrum and $\tilde{u}_{1/3} = 2\tilde{u}_{rms}$ [*Thornton and Guza*, 1983], $\tilde{u}_{rms}$ being the RMS orbital velocity: that is, the square-root of the sum of the u and v variances in the sea-and-swell band.

[22] As waves shoal, they become increasingly nonlinear, typically developing sharper crests, broader troughs, and steeper faces before breaking. Skewness and asymmetry are non-dimensional measures of wave non-linearity, skewness being associated with wave peakedness, asymmetry with the forward or backward pitch of the wave profile [*Elgar and Guza*, 1985]. The skewness of a time series $x(t)$ is given by

$$Sk(x) = \overline{x^3}/\overline{x^2}^{3/2}, \tag{12}$$

and the asymmetry by

$$As(x) = Sk\left[\Im\{H(x)\}\right]. \tag{13}$$

$H(x)$ is the Hilbert transform of x, and $\Im$ denotes the imaginary part. For waves that are pitched forward toward shore, $As < 0$ (i.e., pitched backward in time, and thus forward in space, opposite to the sign convention used by *Elgar and Guza* [1985]). Wave skewness and asymmetry were computed using the $\tilde{u}$ time series.

[23] A quantity of primary interest here is the turbulence intensity close to the bed. The bed level relative to the CDP was determined from the amplitude of the bottom-reflected CDP pulse. Specifically, the range to the seabed was taken as the amplitude-weighted mean of those points with amplitudes greater than 85% of the maximum amplitude of the bottom return, rounded to the nearest millimeter. For each selected run, the time series of these ranges was low-pass filtered (5th-order Butterworth, 0.05 Hz cutoff). The vertical velocities reported are from CDP range bins at heights above the bed level greater than or equal to the 0.7-cm range bin width.

[24] The vertical velocities were partitioned into turbulent and non-turbulent components using a high-pass (5th-order Butterworth) filter with a 0.5 Hz cutoff frequency. This filter decomposition method has been used by several authors with similar cut-off frequencies: 0.7 Hz and 0.8 Hz [*Kos'yan et al.*, 1996]; and 1 Hz [*Foster et al.*, 2000; *Smyth and Hay*, 2002, 2003]. The method has limitations: for example, turbulence in the sea-and-swell band is filtered out, a point to which we return later.

[25] The time series of w' generated by the high-pass filter operation was used to compute the RMS turbulent vertical velocity, $\overline{w'_{rms}}$, for each data run:

$$\overline{w'_{rms}} = \left[\frac{1}{N}\sum_{j=1}^{N} w_j'^2\right]^{1/2} \tag{14}$$

where N is the number of points in a run, and $w_j'^2$ is the turbulence intensity corresponding the jth sample.

[26] To investigate turbulence intensity statistics as a function of wave phase, and in particular the magnitude and wave phase of the peak turbulence intensity during a wave cycle, time series of w'_{rms} were generated by computing the square root of a 9-pt (ca. 0.6-second) running mean of $w_j'^2$. That is,

$$w'_{rmsj} = \left[\frac{1}{9}\sum_{k=-4}^{4} w'^2_{j+k}\right]^{1/2} \tag{15}$$

[27] The peak turbulence level during a given wave, $\hat{w}'_{rms}$, was defined as the maximum value of w'_{rms} block-averaged

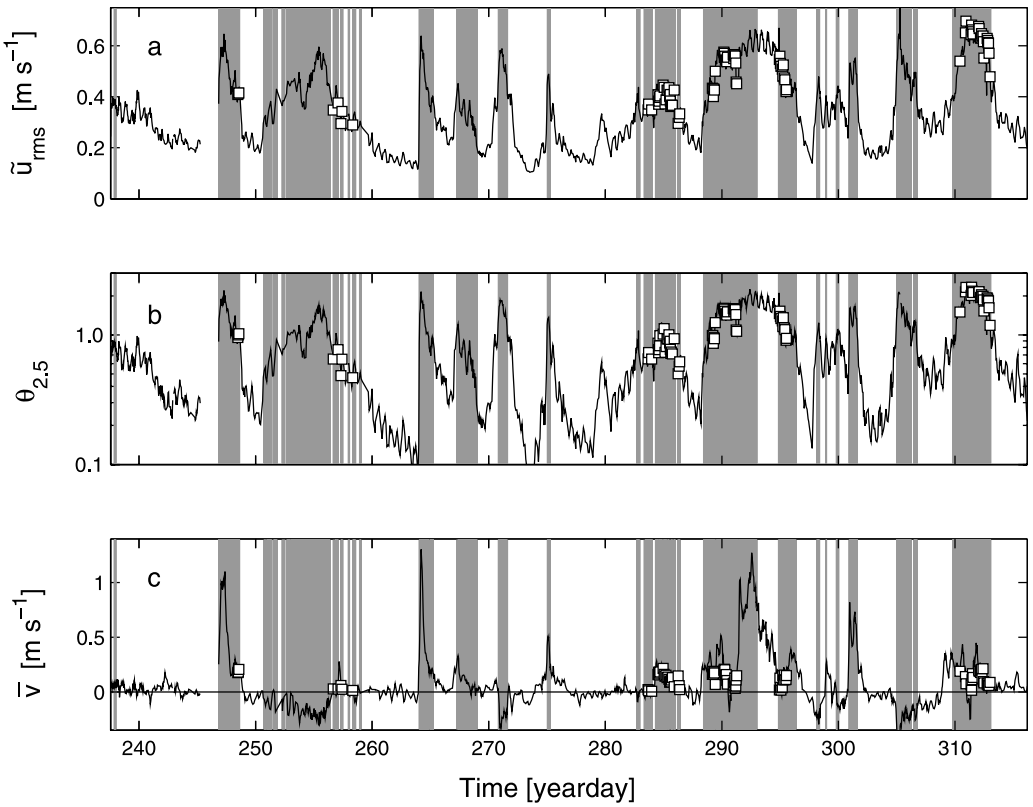

Figure 4. Experiment summary: (a) horizontal RMS velocity during the SandyDuck97 experiment; (b) .grain roughness Shields parameter; (c) mean longshore current. Grey lines indicate data runs during which flat bed conditions were observed at frame C. Squares (□) indicate selected data runs.

in 6-degree wide phase bins. The "significant" ensemble-averaged peak turbulence level was obtained by averaging $\hat{w}'_{rms}$ over the highest-1/3 waves in a run:

$$< \hat{w}'_{rms} >_{1/3} = \frac{1}{M_{1/3}} \sum_{i=1}^{M_{1/3}} \hat{w}'_{rms_i}. \quad (16)$$

$M_{1/3}$ is 1/3 of the number of waves in a run, and the index i represents the ith member of the highest-1/3 waves.

[28] Suspended sediment concentrations were derived from the CDP acoustic backscatter amplitude. The CDP was calibrated in the sediment-laden turbulent jet tank described in *Hay* [1991]. Sand from the frame B site was not available in sufficient quantity, so the calibrations were carried out using quartz sand with the same median size. The resulting linear calibration between the mean square backscatter amplitude and sediment concentration was used to convert the backscatter profile to concentration after correcting for spherical spreading, attenuation in water [*Clay and Medwin*, 1977], and making a single-pass correction for attenuation due to scattering by suspended sediments. Given the possible changes in the median size of the surficial sediments at frame B over the course of the experiment, the resulting concentrations are probably accurate to within better than a factor of 2.

[29] In this study, observed probability distribution functions are compared to theoretical distributions using the quantile-quantile (Q-Q) method [*Levine et al.*, 2001, pp. 202–205]. Data quantiles are plotted against quantiles of the theoretical distribution, and goodness-of-fit is indicated by the coefficient of determination, R^2, of the plotted points relative to the 1:1 line.

3.4. Data Run Selection

[30] Figure 4 presents time series of forcing conditions over the course of the experiment, computed from the ADV data. Plotted in the Figure are: (a) the RMS horizontal velocity in the sea-and-swell band, $\tilde{u}_{rms}$; (b) the grain roughness Shields parameter, $\theta_{2.5}$; and (c) the mean longshore current, $\bar{v}$. The time intervals during which the bed was flat at frame C, based on the fanbeam sonar images from this frame [*Hay and Mudge*, 2005], are indicated by the grey shading. The symbols (□) indicate the data runs selected for the present analysis, based on the following three criteria.

[31] (1) Since we are interested here primarily in high energy wave conditions when the bed is either flat or when small-amplitude, low-steepness ripples are present, only those time periods for which the bed at frame C was flat were considered.

[32] (2) Since we are interested in the friction and turbulence due to waves, and therefore in periods when long-shore currents were small relative to the wave orbital velocities, only runs for which $|\bar{v}| \lesssim 0.25$ m s^{-1} were included. Thus since $\tilde{u}_{1/3} = 2\tilde{u}_{rms}$ for the selected runs was greater than 0.5 m/s (Figure 4) and given condition 1, this second criterion assured that $|\bar{v}| \lesssim 0.5\tilde{u}_{1/3}$. The restriction to weak long-shore currents also served to minimize the obliqueness of wave incidence angles (<13° for the selected runs),

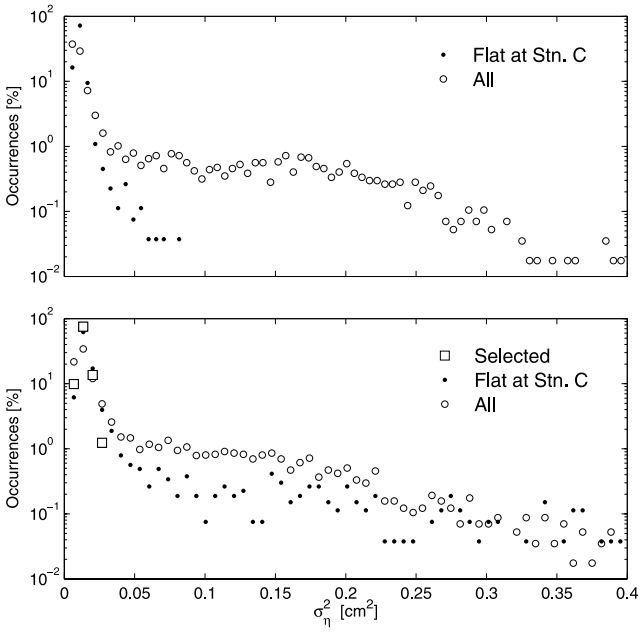

Figure 5. Distributions of bed elevation variance, σ_η^2, at (a) frame C and (b) frame B. Symbols in (a) indicate: distributions for all runs at frame C (○), and runs at frame C identified as flat bed using the frame C fanbeam imagery (●). Symbols in (b) indicate: distributions for all runs at frame B (○); runs at frame B (●) coincident in time with flat bed at frame C; and the selected runs (□). The % values for the selected runs are based on a total of 82, rather than the actual total of 89, as sonar data were not available for 7 of the selected runs.

providing assurance that wakes from the frame legs would not enter the measurement volume of the CDP.

[33] (3) A further restriction to periods of positive (i.e., southward) mean flow was made to ensure that the instrument mast was directed into the long-shore current, thus minimizing the likelihood of frame-generated turbulence entering the measurement volume of the CDP, as discussed earlier.

[34] A total of 89 runs satisfied the three criteria. Note that the grain roughness Shields parameter often exceeded 1 for the selected runs (Figure 4b), indicating the probable occurrence of sheet flow at these times.

4. Results

4.1. Bed Roughness

[35] Cross-shore profiles of bed elevation, η, were obtained from the rotary pencilbeam sonar imagery using analysis methods similar to those described by *Ngusaru and Hay* [2004], at both frames B and C. The elevation profiles were determined over a 2.5- to 3.2-m long x-interval extending from about 1.5 m shoreward to 1.7 m seaward of the sonar position. The profile length changed over time with changing bed elevation under the sensor. The bed elevation spectrum was determined after resampling the bed profile at 1-cm intervals using Hanning-windowed 64-cm segments with 50% overlap. The bed elevation variance, σ_η^2, was obtained by integrating the elevation spectrum from 3 to 15 cpm. The resulting distributions of σ_η^2 are presented in Figure 5.

[36] The occurrence frequencies of σ_η^2 at frame C are shown in Figure 5a for all runs (○), representing the results from over 6000 bed profiles, and for the flat bed runs (●), these being indicated by the fanbeam imagery at frame C [*Hay and Mudge*, 2005]. Note the overlap between the two distributions at low variance (i.e., for σ_η^2 0.025 cm^2). Thus these data indicate a σ_η^2 threshold near 0.025 cm^2, below which the bed at frame C was flat or nearly flat.

[37] The σ_η^2 distribution at frame B is shown in Figure 5b. For all runs (○, again over 6000 in total), the distribution is similar to the all-run distribution at frame C. The solid dots in this figure correspond to frame B runs when the bed at frame C was flat. The non-zero occurrence frequencies for these points at values of σ_η^2 above 0.05 cm^2 indicate that ripples were occasionally present at frame B when the bed at C was flat. For σ_η^2 0.05 cm^2, however, the solid dots again overlap the distribution for all runs. The distribution of the 89 selected runs (□) also falls within this overlap region.

[38] Note that at frame C, σ_η^2 was less than 0.01 cm^2 for approximately 90% of the runs identified as flat bed in the fanbeam imagery. Similarly, the σ_η^2 values at frame B were less than 0.01 cm^2 for 85% of the selected runs. $\sigma_\eta^2 \sim 0.01$ cm^2 would correspond to a sinusoidal ripple amplitude of 1.4 mm. Linear transition ripples, which are low steepness ripples with amplitudes of a few mm [*Dingler and Inman*, 1977; *Crawford and Hay*, 2001], were a frequent occurrence during Sandy-Duck97 at wave energies near the flat bed transition [*Hay and Mudge*, 2005]. These ripples, possibly ephemeral [*Dingler and Inman*, 1977], probably contributed to the bed elevation variance below the 0.025 cm^2 threshold. We will return to the probable occurrence of linear transition ripples in some of the "flat bed" runs later.

4.2. Shields Parameter Distributions

[39] For reasons which become clear as the results are presented, the selected runs were separated into 4 intervals of increasing RMS wave orbital velocity, each interval encompassing roughly the same number of runs to ensure comparable statistical reliability for a given parameter estimate across the four intervals. The 4 intervals are listed in Table 1, together with the corresponding ranges of $\tilde{u}_{rms}$ and grain roughness Shields parameters. Also listed in this table are the interval-averaged values of the peak period, T_p, and the interval-averaged period of the highest-1/3 waves, $T_{1/3}$.

[40] The distributions of the grain roughness Shields parameter, $\theta_{2.5}$ are presented in Figure 6 for the four energy intervals. The distributions for the highest-1/3 waves for Intervals II–IV all peak at $\theta_{2.5} \simeq 0.9$ or more, consistent with the occurrence of flat bed [e.g., *Nielsen*, 1992, p. 140; *Hay and Mudge*, 2005]. The peak of the distribution for Interval I is closer to $\theta_{2.5} = 0.6$, so low-amplitude linear transition ripples [*Dingler and Inman*, 1977; *Conley and Inman*, 1992; *Crawford and Hay*, 2001] are expected to have been present during at least some of the runs in this interval [*Hay and Mudge*, 2005]. $\theta_{2.5}$ exceeds unity for a high proportion of the waves. In particular, for the highest-1/3 waves in Interval IV (Figure 6d), the values of $\theta_{2.5}$ are nearly all greater than 1 and reach a maximum of 3.5,

Table 1. RMS Wave Orbital Velocities, Peak Wave Periods, and Shields Parameters for the Four Sea-and-Swell Band Energy Intervals[a]

		$\tilde{u}_{rms}$, m s^{-1}		T_p, $T_{1/3}$	$\theta_{2.5}$		θ_d	
Interval	No. of Runs	Mean	Range	[s]	Mean	Range	Mean	Range
I	26	0.35	0.28–0.40	11.1 (9.2)	0.67	0.43–0.94	0.56	0.36–0.77
II	22	0.42	0.40–0.46	10.6 (9.1)	0.95	0.84–1.10	0.79	0.70–0.93
III	21	0.52	0.47–0.55	11.4 (9.0)	1.34	1.08–1.49	1.13	0.91–1.26
IV	20	0.60	0.53–0.64	10.0 (9.2)	1.77	1.45–2.08	1.50	1.22–1.76

[a]Both the interval-averages and ranges are listed.

indicating a high likelihood that sheet flow occurred during all of the runs in this interval.

4.3. Near-Bed Turbulence

[41] Representative time series showing velocity and suspended sediment concentrations on wave-period timescales are presented in Figure 7 for a 60-s segment from a moderately high-energy data run (i.e., a run from Interval III). Cross-shore velocities from the ADV, representing the free-stream velocity, are presented in panel 7a. The data in panels 7b and c are from the CDP and are respectively time series of turbulence intensity for the three range bins closest to the bottom, and of suspended sediment concentrations at ranges within 20 cm of the bed. These data indicate a sharp increase in near-bed turbulence close to wave crests, with peak values occurring at or slightly after the crest, followed by rapid decay to near background levels before the arrival of the next crest. The suspended sediment concentrations exhibit a similar pattern, with the onset of major suspension events roughly coinciding with the onset of enhanced near-bed turbulence. The elevated levels of both turbulence and suspended sediment concentration are largely confined to the 3 to 5 range bins nearest the bed. (Note in passing that this contrasts sharply with comparable field data over rippled beds, which exhibit turbulence and sediment suspension reaching heights of 10s of cm for comparable-period but smaller-amplitude waves: see *Smyth et al.* [2002], Figure 2.)

[42] The CDP data in Figure 7 indicate that, for these nominally flat bed conditions, w'_{rms} decays rapidly following the passage of a wave crest. Also, the peak turbulence values for individual waves are roughly symmetric about the largest wave in the group, much like the temporal pattern of peak horizontal wave orbital velocities. Thus these data indicate that turbulence generated at the bed under a given wave crest was largely independent of that generated under the crest of the preceding wave.

[43] This point is further demonstrated in Figure 8, in which the occurrence of the peak RMS turbulent velocity, $\hat{w}'_{rms}$, for the highest-1/3 waves in the selected runs is

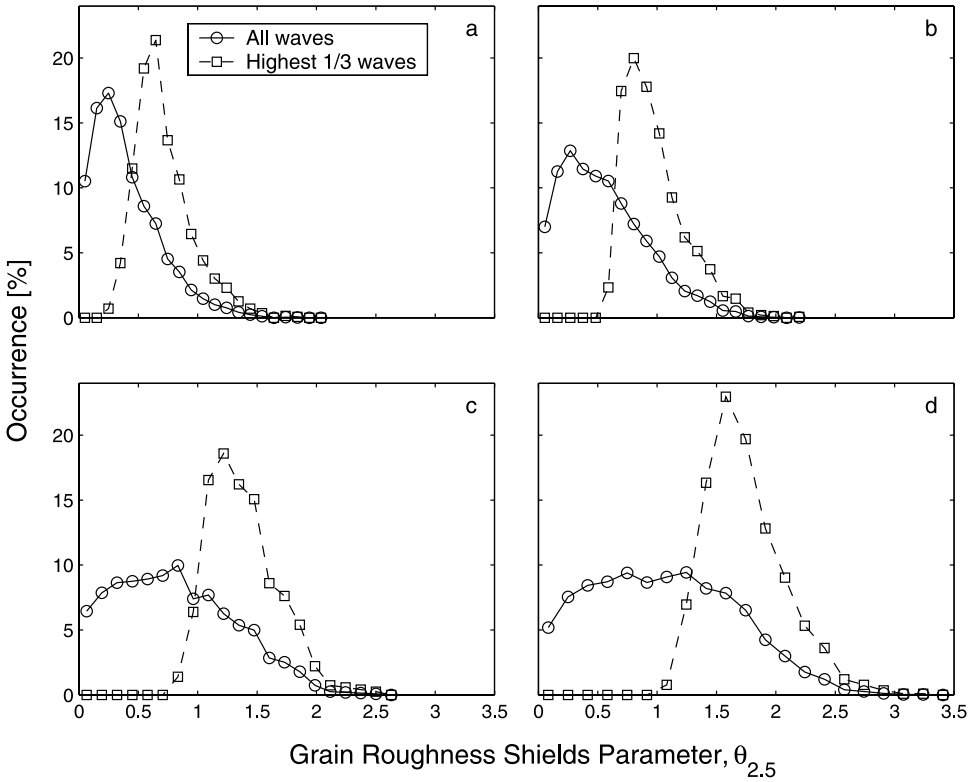

Figure 6. Distributions of grain roughness Shields parameters for the four energy intervals listed in Table 1 for all waves (○) and for the highest-1/3 waves (□) in the 89 selected data runs. Numbers of points on which distributions for all (highest-1/3) waves are based are: (a) 4307 (1428); (b) 3854 (1280); (c) 3692 (1222); (d) 3513 (1164). Data are based on the cross-shore velocity component.

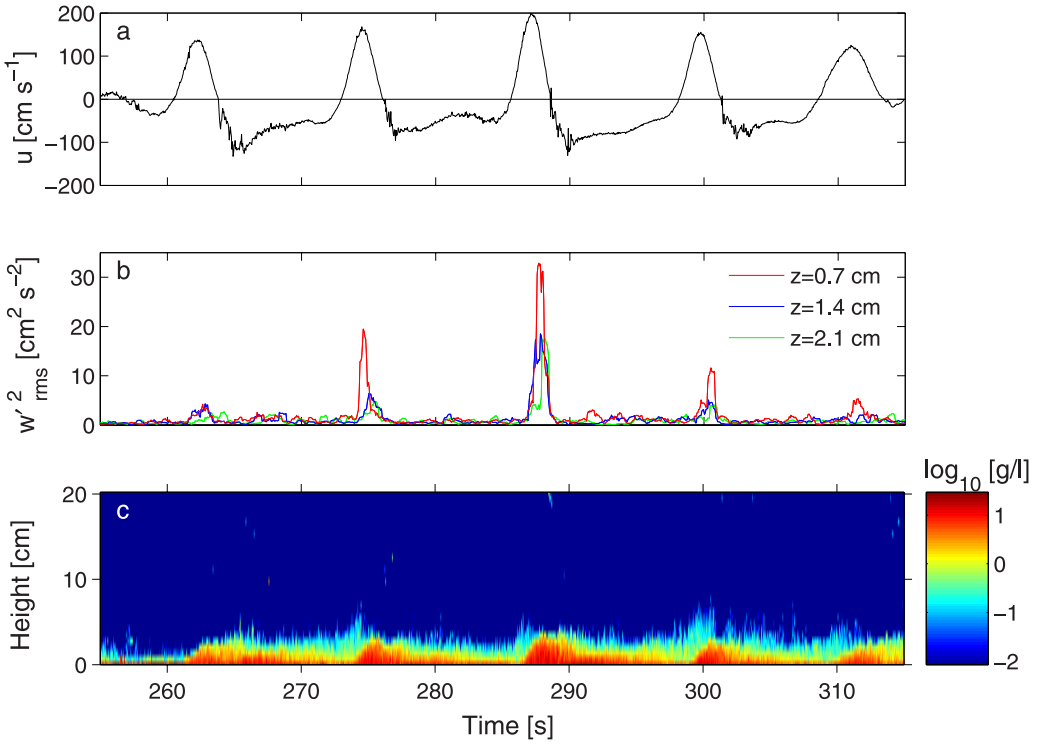

Figure 7. (a) ADV cross-shore velocity for a 1-minute segment of the SandyDuck97 experiment; (b) time series of vertical turbulence intensity in the CDP bins immediately above the bed (0.7 to 2.1 cm above bottom); (c) vertical profiles of suspended sediment concentration. Time is in seconds after the start of the data run.

plotted relative to wave phase. There is a clear association between $\hat{w}'_{rms}$ and wave crests, and only infrequent occurrences of $\hat{w}'_{rms}$ under the troughs. Figure 8b presents the percent occurrence of $\hat{w}'_{rms}$ as a function of wave phase, again for the highest-1/3 waves. Based on this figure, the range of phases corresponding to peak turbulence under wave crests was defined to be $-40° \leq \phi \leq 115°$; wave troughs include all phases outside this range. Using this definition, approximately 72% of turbulence peaks occurred under wave crests, with a mean phase of $\hat{\phi} = 32°$ and magnitudes ranging from 0.9 to 12.2 cm s^{-1}.

[44] Averaging $\hat{w}'_{rms}$ and $\hat{\phi}$ over the highest-1/3 waves in each run yields $<\hat{w}'_{rms}>_{1/3}$ and $<\hat{\phi}>_{1/3}$. These quantities are plotted in Figure 8c, and clearly illustrate the tendency for higher peak turbulence levels at a fixed height to occur earlier in the wave cycle. On the basis of the best fit line, the highest peak turbulence values occurred near zero phase (i.e., shortly after the wave crest), and approximately 45° earlier than the lowest peak energies. (The minimum value of $<\hat{\phi}>_{1/3}$ in Figure 8c is 10°, the maximum 55°.)

[45] The wave phase at which w'_{rms} peaks can be compared to the laboratory measurements made by *Sleath* [1987] and *Jensen et al.* [1989] in sinusoidal oscillatory flow above fixed-grain rough bottom boundaries using Laser Doppler Anemometry (LDA). Specifically, Figure 26c in *Jensen et al.* [1989] shows vertical profiles of w'_{rms} versus wave phase. These profiles indicate turbulence at the bed developing in advance of the wave crest initially, and then diffusing upward away from the bottom as wave phase advances. Comparable behavior is exhibited even more clearly in Sleath's Figure 2, in which phase-averaged time series of w'_{rms} are plotted at different heights. These laboratory results are consistent with the general physical understanding of the temporal development of wave bottom boundary layers over flat beds: that is, the maximum stress at the bed typically leads the wave crest, and turbulence diffuses upward away from the bed. *Jensen et al.* [1989] plot their data against a non-dimensional vertical coordinate corresponding to z/A here. For our results at z = 0.7 cm, a representative value of $z/A_{1/3}$ is 0.004 (using $\tilde{u}_{1/3} = 2\tilde{u}_{rms}$ = 1 m s^{-1} and T_p = 10 s, Table 1). At this non-dimensional height, the w'_{rms} values in Figure 25c of *Jensen et al.* [1989] peak 15 to 30° after the wave crest. Similarly, the results in Sleath's Figure 11 indicate that $\hat{w}'_{rms}$ occurs at $\phi \sim 10°$ for $z/A = 0.004$, with the abscissa converted to z/A using the values in his Table 1. Thus the occurrence of peak near-bed turbulence at or shortly after the wave crest observed in the present field measurements above a mobile bed is also exhibited by laboratory measurements above rough beds composed of fixed grains.

[46] Figure 9a shows the variation of w'_{rms} with wave phase, ensemble-averaged over the highest-1/3 waves in Interval IV, at the heights of the three range bins nearest the bed. At all three heights, w'_{rms} peaks after the wave crest. With increasing height, the peak decreases in amplitude and occurs at progressively later phases (i.e., at ϕ_{max} = 15°, 21° and 27° respectively), consistent with diffusive growth of the WBL. The wave-phase variation of w'_{rms} at 0.7-cm height for all four wave-energy intervals is shown in Figure 9b: ϕ_{max} occurs earlier for Interval IV (at 15°), and later (at 27°) for the three lower-energy intervals.

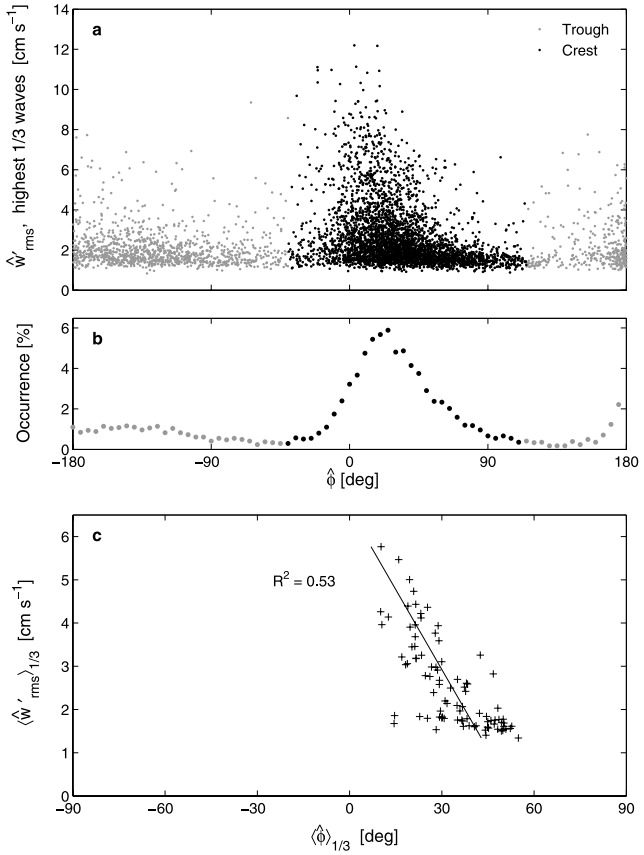

Figure 8. (a) Peak turbulence level $\hat{w}'_{rms}$ versus the wave phase, $\hat{\phi}$, at which $\hat{w}'_{rms}$ occurred, for the highest-1/3 waves in the selected runs. (b) The distribution of $\hat{\phi}$. The black points in (a) and (b) lie in the interval $-40° \leq \hat{\phi} \leq 115°$, and together indicate the predominant occurrence of peak turbulence under wave crests. (c) The average of $\hat{w}'_{rms}$ and $\hat{\phi}$ over the highest-1/3 waves in each run with -40° $\leq \phi \leq$ 115° (+). Data in all panels are from the first CDP bin immediately above the bed (z = 0.7 cm). ϕ = 0 corresponds to wave crests.

[47] In their laboratory investigation of oscillatory flow above a *smooth* bed, *Jensen et al.* [1989] found that ϕ_{max} decreased with increasing wave Reynolds number. The wave Reynolds numbers here, defined as $Re_{1/3} = A_{1/3}\tilde{u}_{o_{1/3}}/\nu$, range from 4×10^5 to 2.4×10^6 for the four energy intervals (Table 2). Jensen et al. found that the RMS fluctuations in the bed shear stress (measured directly with a hot-film shear stress probe) peaked at progressively earlier phases (decreasing from 45° to about -30°) as the wave Reynolds number increased from 1.6×10^5 to 1.6×10^6 [*Jensen et al.*, 1989, Figure 10]. This Reynolds number range is comparable to the range of $Re_{1/3}$ in Table 2. Thus the variations of ϕ_{max} with Interval in Figure 9b could be interpreted as a manifestation of the variation with wave Reynolds number of the phase at which transition to turbulence occurs. The fact that ϕ_{max} is the same for Intervals I to III could be due in part to the probable occurrence of linear transition ripples in Interval I (see below, and section 4.5). It is worth noting that the effect of wave Reynolds number on the phase of maximum bed stress over smooth beds is supported by numerical models of the turbulent WBL. In direct numerical simulations (DNS) at $Re = 3.2 \times 10^5$ and 5×10^5 [*Spalart and Baldwin*, 1987; see also *Jensen et al.*, 1989], the phase of maximum bed stress decreased from about 10° to −10°. Similarly, *Chang and Scotti* [2006] show via large eddy simulations (LES) that the peak turbulent kinetic energy in the WBL for sinusoidal oscillatory flow over a smooth bed occurs near $\phi \sim 45°$ at a wave Reynolds number of 2×10^5, similar to the ∼45° phase observed by *Jensen et al.* [1989] for the onset of turbulence over a smooth bed at $Re \sim 10^5$.

[48] The laboratory data for rough beds do not exhibit a pronounced trend for ϕ_{max} versus Re (see, for example, *Sleath* [1987] Figure 9, except possibly the data for the roughest bed). Sleath's results indicate values for ϕ_{max} nearest the bed ranging from ca. -25° to ca. +25°, and considerable scatter within this range. Note that Sleath's wave Reynolds numbers are relatively low in the present context, being less than 3.5×10^5. The *Jensen et al.* [1989] rough bed experiments were carried out at Reynolds numbers of 1×10^6 to 6×10^6, but variations of ϕ_{max} with Re

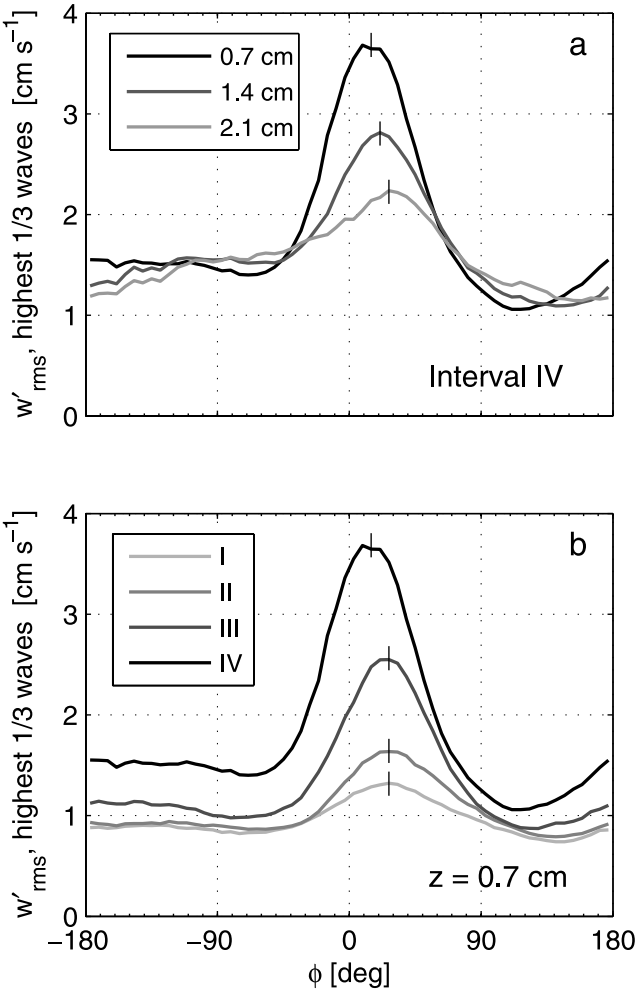

Figure 9. w'_{rms} versus wave phase for the highest-1/3 waves. (a) For Interval IV, and the 3 bins nearest the bed. (b) For all four intervals, at 0.7-cm height. ϕ = 0 corresponds to wave crests. The vertical bars indicate ϕ_{max} determined from smoothed versions of the curves shown.

Table 2. Wave Reynolds Numbers, RMS Infragravity Wave Velocities, Mean Cross- and Along-Shore Velocities, and Current/Wave Ratios for the Four Sea-and-Swell Band Energy Intervals[a]

	$Re_{1/3}$ ($\times 10^6$)		$\tilde{U}_{rms}$, m s^{-1}		$-\bar{u}$, m s^{-1}		$\bar{v}$, m s^{-1}		$\sqrt{\tilde{u}^2+\tilde{v}^2}/\tilde{u}_{1/3}$	
Interval	Mean	Range	Mean	Range	Mean	Range	Mean	Range	Mean	Range
I	0.87	0.51–1.26	0.08	0.06–0.12	0.04	0.01–0.08	0.10	0.01–0.18	0.15	0.04–0.28
II	1.21	0.60–1.69	0.11	0.08–0.18	0.05	0.01–0.15	0.14	0.05–0.22	0.19	0.07–0.27
III	1.90	1.34–2.25	0.16	0.13–0.23	0.09	0.02–0.21	0.10	0.02–0.21	0.14	0.04–0.24
IV	2.21	1.75–2.78	0.22	0.17–0.28	0.20	0.07–0.30	0.12	0.01–0.21	0.20	0.08–0.31

[a]Both the interval-averages and ranges are listed.

were not reported. Nonetheless, Sleath's rough-bed results when compared to those obtained by Jensen et al. for smooth beds indicate that transition to turbulence occurs earlier in the wave cycle when the bed is rough. Given the well-known effect of roughness on the critical Reynolds number for transition to turbulence in unidirectional-flow boundary layers, this shift to earlier phases is reasonable. The shift does however suggest a possible explanation for the similarity among the values of ϕ_{max} in Intervals I to III, since linear transition ripples would have been present in Interval I and probably also at least intermittently in Interval II, resulting in reduced values of ϕ_{max}.

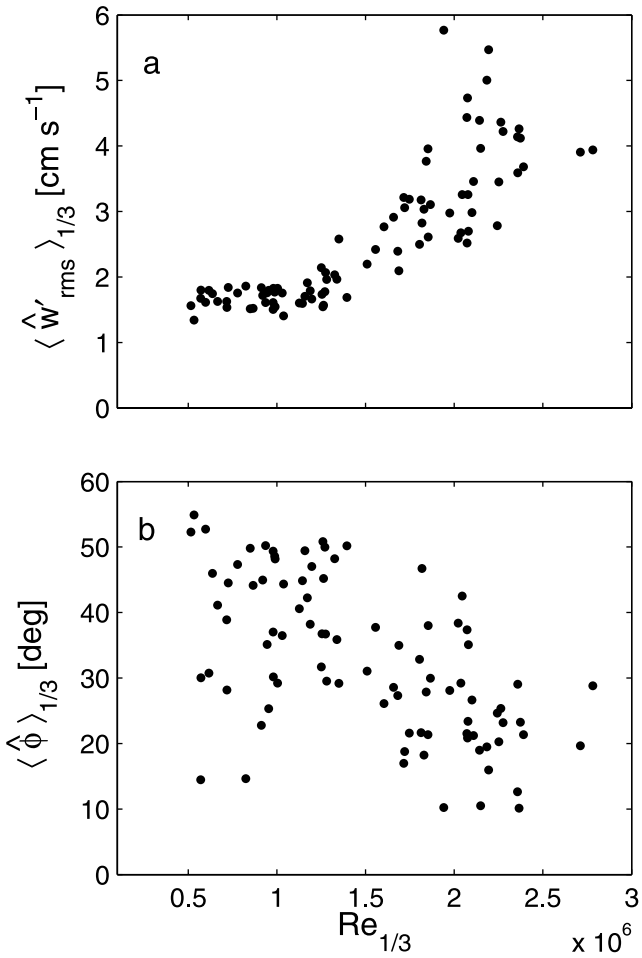

Figure 10. (a) Peak turbulence versus wave Reynolds number, averaged over the highest-1/3 waves in each run. (b) The wave phase at which peak turbulence occurred, averaged over the highest-1/3 waves in each run, versus wave Reynolds number.

[49] The observed values of $<\hat{w}_{rms}'>_{1/3}$ and $<\hat{\phi}>_{1/3}$ are plotted versus *Re* in Figure 10. For $Re \lesssim 1.2 \times 10^6$, *peak* turbulence intensities for the highest-1/3 waves were relatively constant, consistent with the *Smyth and Hay* [2003] result that RMS near-bed turbulence intensities remain nearly independent of rippled bed state (implying that bottom stress also remains constant). At $Re \sim 1.2 \times 10^6$, however, the peak turbulence intensities in Figure 10a abruptly begin to increase with increasing *Re*. The corresponding phases, $<\hat{\phi}>_{1/3}$, are plotted in Figure 10b and while exhibiting the decrease with increasing *Re* discussed above, there is no evidence of a sharp change in phase at $Re \sim 1.2 \times 10^6$.

[50] The values of skewness and asymmetry for the four Intervals are listed in Table 3. Skewness was relatively high, with average values increasing slightly from 0.67 for Interval I to 0.85 for Interval IV. In contrast, the values of wave asymmetry were uniformly small, 0.06 or less in magnitude on average. These ranges of $Sk_{\tilde{u}}$ and $As_{\tilde{u}}$ are consistent with previously reported values from the SandyDuck97 experiment [*Herbers et al.*, 2003; *Hay and Mudge*, 2005]. The 3rd-order statistics are also consistent with the time series of *u* in Figure 7, which is positively skewed relative to the time axis and exhibits comparatively less asymmetry about the ordinate. Note also with respect to the turbulence signal that, unlike the sinusoidal wave case, in which a turbulence intensity maximum occurs in each half cycle [*Sleath*, 1987; *Jensen et al.*, 1989; *Chang and Scotti*, 2006], the high skewness of these waves is reflected in the turbulence signal by the appearance of a single pronounced peak during each full wave cycle.

[51] Correlations between $<\hat{w}'_{rms}>_{1/3}$ and the 2nd and 3rd moments of the wavefield are listed in Table 4. $<\hat{w}'_{rms}>_{1/3}$ is well-correlated with $\tilde{u}_{rms}$ ($R^2 = 0.78$), but weakly correlated with the 3rd-order moments (R^2 values of 0.13 or less). Thus the results in Table 4 suggest that the higher peak turbulence levels were associated with waves of higher energy, but were not strongly dependent on wave nonlinearity. This is the first of several indicators that the magnitude of the near-bed turbulence intensity was relatively unaffected by wave non-linearity.

Table 3. Skewness and Asymmetry for the Four Sea-and-Swell Band Energy Intervals[a]

	$Sk_{\tilde{u}}$		$As_{\tilde{u}}$	
Interval	Mean	Range	Mean	Range
I	0.67	0.25–1.14	0.00	−0.15–+0.21
II	0.71	0.32–1.17	0.05	−0.15–+0.20
III	0.75	0.27–1.26	0.06	−0.09–+0.37
IV	0.85	0.61–1.15	−0.05	−0.15–+0.11

[a]Both the interval-averages and ranges are listed.

Table 4. Coefficients of Determination, R^2, for Correlations Between the Magnitude and Phase of Peak Near-Bed Turbulence Under Wave Crests and the 2nd and 3rd Moments of the Sea-and-Swell Waves

	R^2		
	$\tilde{u}_{rms}$	$Sk_{\tilde{u}}$	$As_{\tilde{u}}$
$\langle \hat{w}'_{rms} \rangle_{1/3}$	0.78	0.13	0.02

4.4. The Probability Distributions of w'_{rms} and $\hat{w}'_{rms}$

[52] The observed probability distributions of w'_{rms} and $\hat{w}'_{rms}$ for the range bin nearest the bed (0.7-cm height) are indicated by the plotted points in Figures 11a–11d for each of the four wave energy intervals. As energy increases (i.e., through Intervals I to IV in panels 11a through d), the peaks in the distributions shift to progressively higher values, as expected given the correlations between peak turbulence and wave energy discussed previously. Note as well the increase in the width of the distributions with increasing wave energy, and that this increased width is most pronounced for Interval IV. We return to this point later.

[53] The solid lines in Figure 11 represent the Gamma distribution, for which the probability density P is given by,

$$P(y) = \frac{1}{b^a \Gamma(a)} y^{a-1} \exp[-y/b] \qquad (0 \le y < \infty), \qquad (17)$$

where Γ denotes the Gamma function. The parameters a and b are related to the mean, $\bar{y}$, and variance, σ_y^2, by $a = \bar{y}^2/\sigma_y^2$ and $b = \sigma_y^2/\bar{y}$ [*Papoulis*, 1965, p. 147]. The curves in Figure 11 represent equation (17) with $y = w'_{rms}$, and with a and b determined by the mean and variance of the solid points. Thus the curves are not best fits in the usual sense (the R^2 results from least squares Q-Q fits are discussed below). The Gamma distribution represents the w'_{rms} data well. As demonstrated in the following analysis, this result is due to a combination of turbulent velocities being Gaussian-distributed and the data processing steps used to determine w'_{rms}.

[54] It is well known that velocity fluctuations at a fixed point in homogeneous turbulence are normally distributed [e.g., *Batchelor*, 1953, pp. 169–170]. In the present study, RMS turbulent velocities were estimated from a 9-point running mean of the vertical turbulence intensity (see section 3.3, equation (15)). Given a Gaussian parent distribution with constant variance and zero mean (the zero-mean is assured by the high-pass filter operation, the constant variance is an assumption), these mean square velocities would then be chi-square-distributed, with 9 degrees of freedom: i.e., $P(y) = \chi^2_{\mathrm{N}}(y)$, with $y = w'^2$ and $N = 9$.

[55] We are interested in the distribution of the RMS velocity. Let ξ be a Gaussian-distributed random variable with unit variance, and construct a random variable ξ_{rms} as the square-root of the mean of N values of ξ^2. The theoretical probability density of ξ_{rms} can be written explicitly as

$$P(y) = 2yN\chi^2_N(y) \qquad (y = \xi_{rms}). \qquad (18)$$

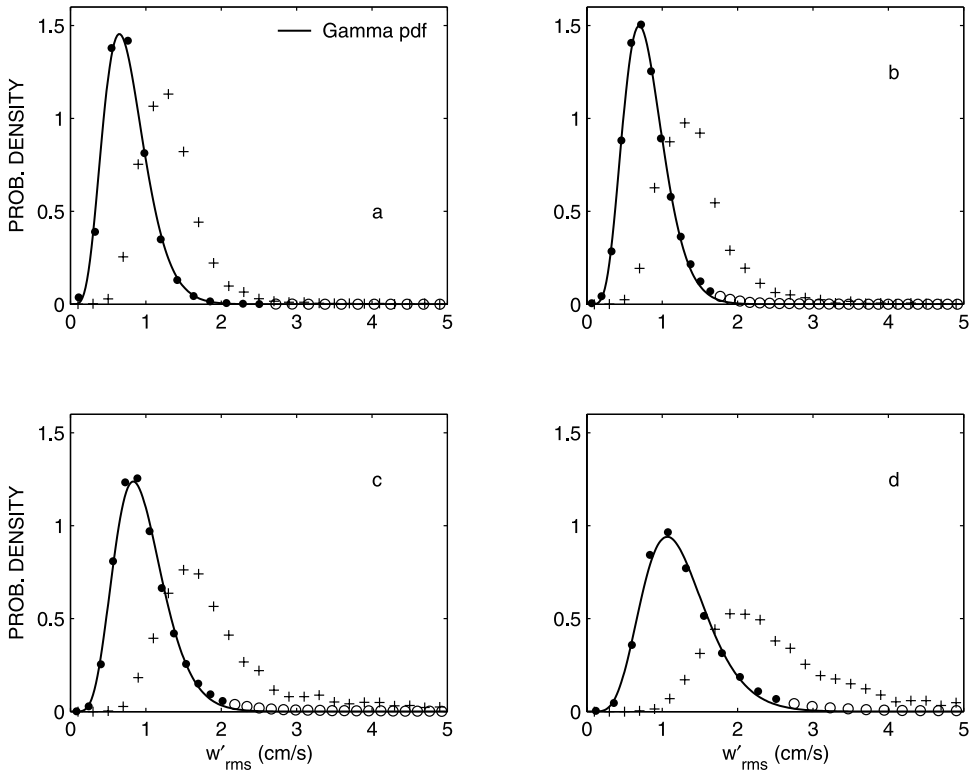

Figure 11. Probability distributions of RMS turbulent velocity, w'_{rms} (●, ○) for all waves, with fitted Gamma distributions. Panels a through d represent the four wave energy intervals (Table 1). The solid curves represent Gamma distributions with the same mean and variance as the points represented by the solid circles. Distributions for $\hat{w}'_{rms}$ are also shown (+). Data are from the CDP bin immediately above the bed (z = 0.7 cm).

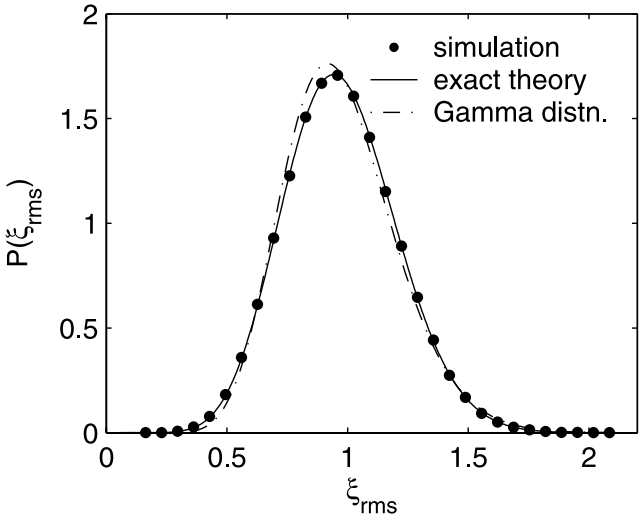

Figure 12. Probability distribution of a simulated RMS signal, ξ_{rms}, computed (in the same way as w'_{rms}) from Gaussian-distributed random noise. The solid points indicate the simulation results; the solid and dash-dot curves are the probability density functions for the exact theory and the Gamma distribution, respectively.

This equation is compared in Figure 12 to $P(\xi_{rms})$ obtained from a computer simulation using a normally distributed random variable ξ and following the same steps to obtain ξ_{rms} as were used to determine w'_{rms} from the data. The agreement between theory and simulation is very good. Included in the figure is the corresponding Gamma distribution, which also provides a good fit.

[56] The distributions of w'_{rms} were also examined in the three CDP bins immediately above $z = 0.7$ cm height. For all four bins, w'_{rms} was found to be well-represented by the Gamma distribution, with goodness-of-fit R^2 values (derived from Q-Q plots as described in section 3.3) ranging from 0.92 to 0.95.

[57] Thus the results in this section indicate that: (a) w'_{rms} is Gamma-distributed to a good approximation; (b) that, given the data processing steps used to determine w'_{rms}, the good fit to a Gamma probability density is consistent with turbulent velocities being Gaussian; (c) that the w'_{rms} distribution for Interval IV is significantly broader than for the 3 lower energy intervals; and (d) this increased breadth is even more pronounced for $\hat{w}'_{rms}$.

4.5. Wave Friction Factors

[58] Run-averaged wave friction factors were computed using $\overline{w'_{rms}}$ as follows:

$$f_w = 2\left(\frac{2\Lambda\overline{w'_{rms}}}{\tilde{u}_{rms}}\right)^2, \tag{19}$$

with

$$\tilde{u}_{rms} = \left[\sigma_{\tilde{u}}^2 + \sigma_{\tilde{v}}^2\right]^{1/2}, \tag{20}$$

where $\sigma_{\tilde{u}}^2$ and $\sigma_{\tilde{v}}^2$ are the variances of the alongshore and cross-shore velocity components in the sea-and-swell band. To obtain equation (19), $\tilde{u}_o$ in equation (11) has been replaced by the significant wave orbital velocity $2\tilde{u}_{rms}$, and w'_{rms} has likewise been replaced by a "significant" estimate, $2\overline{w'_{rms}}$.

[59] The run-averaged f_w values estimated from equation (19) are plotted in Figure 13, together with several model-predicted curves for 0.17-mm diameter sand. Note that almost all of the data points fall within the region bounded by the model predictions. Note also that, for $0.4 \lesssim \theta_d \lesssim 1$, the general curvature exhibited by the observations is similar to that of the Tolman-predicted curve. Concave-upward curvature over this θ_d range is encouraging, as it reflects the expected decrease in ripple steepness with increasing θ_d until the bed becomes truly flat at $\theta_d \sim 0.8$ to 1, and the increased relative roughness due to sheet flow for $\theta_d > 1$. (In Figures 13 and 14, θ_d was computed using equation (8) with $\tilde{u}_o$ replaced by $\tilde{u}_{1/3} = 2\tilde{u}_{rms}$, $\tilde{u}_{rms}$ being given by equation (20), and f_d by equation (7) with $r = d_{50}$ and A set equal to $A_{1/3} = \tilde{u}_{1/3}/\omega$).

[60] The data points in the figure were obtained using $\Lambda = 1.3$ and 1.7, values that are based on extrapolating the inertial subrange to 0.1 Hz from the 0.5-Hz cutoff frequency used to obtain $w'(t)$ (see section 3.3), in order to account for the turbulent energy in the sea-and-swell band. Explicitly, with a power law form for the vertical velocity spectral density $S_{ww} \propto f^{\zeta}$ in the inertial subrange,

$$\Lambda = \left[\int_{f_{Lo}}^{f_{Hi}} S_{ww}df \Big/ \int_{f_c}^{f_{Hi}} S_{ww}df\right]^{1/2} = \left[\frac{f_{Hi}^{1+\zeta} - f_{Lo}^{1+\zeta}}{f_{Hi}^{1+\zeta} - f_{f_c}^{1+\zeta}}\right]^{1/2} \tag{21}$$

where $f_c = 0.5$ Hz is the filter cutoff frequency, $f_{Lo} = 0.1$ Hz is the limit of extrapolation into the sea-and-swell band, and f_{Hi} is the upper limit of integration. With f_{Hi} set equal to 50 Hz (higher values make little difference) and invoking the usual $-5/3$ slope for the inertial subrange, equation (21) yields $\Lambda = 1.74$. However, as *Smyth and Hay* [2003] have shown, the vertical velocity spectrum in the inertial subrange is less steep than $-5/3$ for measurement points close to the bed. A value of $\zeta = -4/3$ is representative of their spectra, and gives $\Lambda = 1.38$.

[61] Thus the values of Λ used to produce the f_w data points in Figure 13 were based on estimates of the likely lower and upper limits for the contribution to the total vertical turbulent kinetic energy from the sea-and-swell band. It can be seen from the figure that the points based on the lower limit ($\Lambda = 1.3$) just meet the predicted curves for the fixed-grain, flat bed case at intermediate values of the Shields parameter ($0.8 \lesssim \theta_d \lesssim 1$), while points based on $\Lambda = 1.7$ in the same θ_d range are clustered about the Tolman curve. Both of these results are encouraging, suggesting that the chosen upper and lower limits for Λ are reasonable.

[62] At the higher values of θ_d, f_w increases more rapidly than the Tolman curve. With reference to Table 1, it is seen that the region of more rapid increase largely coincides with Interval IV. Recall that the w'_{rms} distribution function was broadest for this interval, reflecting more energetic turbulence. We return to this point later.

[63] Wave friction factors were also calculated for each run using peak RMS turbulent velocities and orbital velocity amplitudes averaged over the highest-1/3 waves, as follows:

$$\hat{f}_w = \frac{1}{M_{1/3}} \sum_{i=1}^{M_{1/3}} 2\frac{(2\Lambda\hat{w}'_{rms_i})^2}{\tilde{u}_{ox_i}^2}, \tag{22}$$

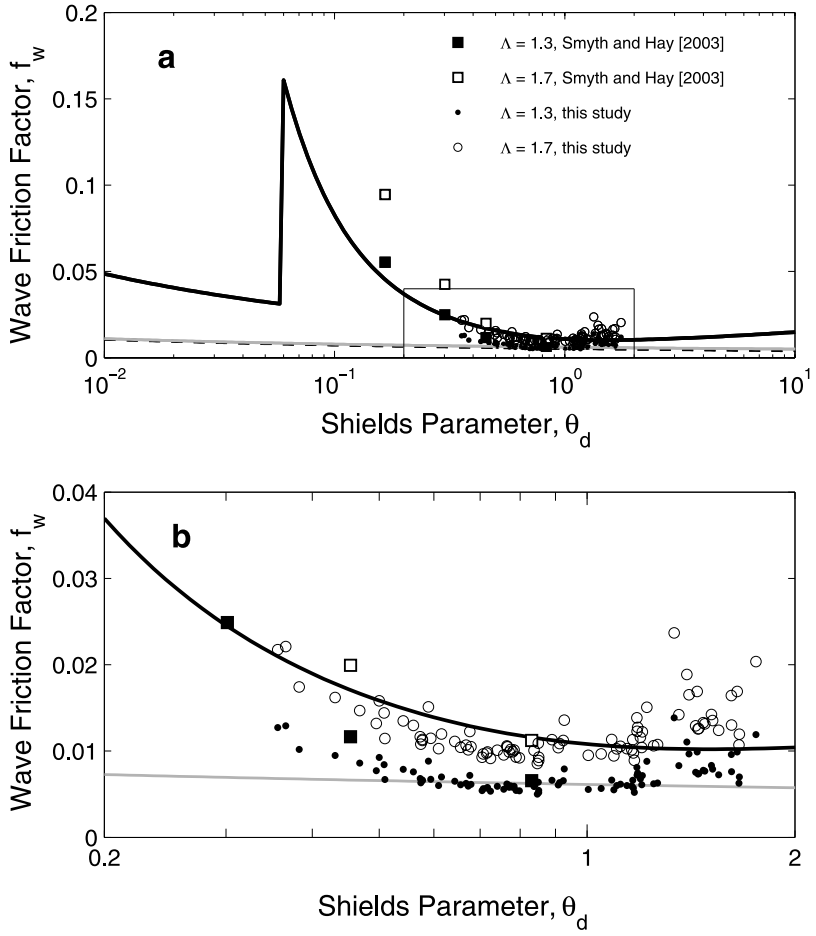

Figure 13. Wave friction factors as a function of grain roughness Shields parameter. The inset region in (a) is expanded in (b). The curves are different model predictions for grain diameter $d = 0.17$ mm: *Tolman* [1994] (solid black); *Tolman* [1994] with $k_N = d$ (dashed black); and *Swart* [1974] with $r = d$ (solid grey). The symbols indicate run-averaged friction factors (equation (11)) for $\Lambda = 1.3$ (solid) and 1.7 (open), respectively, including the *Smyth and Hay* [2003] values (adjusted from $\Lambda = 1$).

where $\tilde{u}_{ox_i}$ is the cross-shore velocity amplitude of the ith wave, $M_{1/3}$ is 1/3 of the number of waves in the run, and the index i represents the ith member of the highest-1/3 waves, as in equation (16). $\hat{f}_w$ is plotted against f_w in Figure 14, for $\Lambda = 1.7$. The values of $\hat{f}_w$ and f_w are very similar for θ_d 0.8. Above this value of θ_d, the two estimates remain proportional on average, but the $\hat{f}_w$ values are roughly a factor of 2 larger.

[64] Referring to equation (22), $\hat{f}_w$ is based on a direct estimate of the "significant" wave stress, i.e., the maximum stress averaged over the highest-1/3 waves. In contrast, f_w in equation (19) is based on $\overline{w'_{rms}}$, which is determined from the variance of w' over the full duration of a run and thus represents an average over all waves. Consequently, using this f_w to determine the significant wave stress depends upon the relative behavior of the high-amplitude tails of the w'_{rms} and $\tilde{u}_{rms}$ distributions. Explicitly, with $\tilde{u}_{1/3} = 2\tilde{u}_{rms}$ and similarly $< \hat{w}'_{rms} >_{1/3} = 2\overline{w'_{rms}}$, equation (19) remains unchanged: that is, f_w estimates based on $\tilde{u}_{1/3}$ and $< \hat{w}'_{rms} >_{1/3}$ would be given by

$$f_w = 2\left(\frac{2\Lambda < \hat{w}'_{rms} >_{1/3}}{\tilde{u}_{1/3}}\right)^2 = 2\left(\frac{2\Lambda\overline{w'_{rms}}}{\tilde{u}_{rms}}\right)^2. \qquad (23)$$

However, the assumption that the average over the highest-1/3 amplitudes is twice the square-root of the variance of the input time series holds if the amplitudes are Rayleigh-distributed. We have already seen that w'_{rms} is very nearly

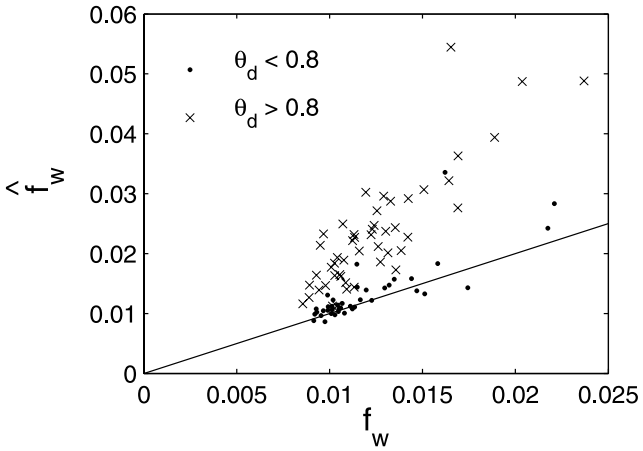

Figure 14. Peak wave friction factors, $\hat{f}_w$, vs. f_w. The symbols represent $\theta_d \leq 0.8$ (•) and >0.8 (×), respectively, as indicated. $\Lambda = 1.7$.

Table 5. Interval-Averaged Values (±Standard Deviation) of Wave Friction Factors and Friction Velocities, for $\Lambda = 1.7$ and $B = 4.91$ (Equation 40)

Interval	f_w	f_{wB}	$\hat{f}_w$	$u_{*_{1/3}}$, cm s^{-1}	$u_{*B_{1/3}}$, cm s^{-1}	$\hat{u}_{*_{1/3}}$, cm s^{-1}
I	0.013 ± 0.003	0.012 ± 0.003	0.015 ± 0.006	5.6 ± 0.3	5.4 ± 0.2	5.8 ± 0.7
II	0.010 ± 0.001	0.009 ± 0.001	0.012 ± 0.003	6.0 ± 0.5	5.7 ± 0.5	6.5 ± 1.0
III	0.011 ± 0.001	0.010 ± 0.001	0.019 ± 0.004	7.6 ± 0.6	7.2 ± 0.6	9.8 ± 1.1
IV	0.015 ± 0.003	0.013 ± 0.003	0.031 ± 0.010	10.0 ± 1.1	9.5 ± 1.0	14.0 ± 2.2

Gamma-distributed. Based on the simulations used for Figure 12,

$$< \hat{\xi}_{rms} >_{1/3} = 1.7\sigma_\xi, \tag{24}$$

where σ_ξ is the square-root of the variance of ξ, and the left-hand side is the mean of the highest-1/3 of the peak values from successive segments of ξ_{rms}. (These segments were 200 points long, corresponding to the roughly 200 w' data points in a 10-s wave.) Using the actual turbulence data, we found that $< \hat{w}'_{rms} >_{1/3}$ was 2 to 3 times greater than $\overline{w'_{rms}}$. Thus $< \hat{w}'_{rms} >_{1/3} \sim 2\overline{w'_{rms}}$. The question as to whether the factor of 2 holds for $\tilde{u}_{1/3}$ is examined in the next section.

[65] The mean values of the friction factor estimates for the four energy intervals, and the associated mean friction velocities, are listed in Table 5. (Note that f_{wB} and $u_{*B_{1/3}}$ are introduced in section 5.4.)

4.6. Orbital Velocity Amplitude Distributions

[66] The probability density of the amplitudes of deep-water surface gravity waves is closely represented by the Rayleigh distribution [*Longuet-Higgins*, 1952]. The Rayleigh distribution for the orbital velocity amplitude is given by

$$P(\tilde{u}_o) = \frac{2\,\tilde{u}_o}{\tilde{u}^2_{o_{rms}}} \exp\left[\frac{-\tilde{u}_o}{\tilde{u}_{o_{rms}}}\right]^2 \tag{25}$$

where $\tilde{u}_{o_{rms}}$ is the RMS value of the orbital velocity amplitude, $\tilde{u}_o$. In the near-shore zone, *Thornton et al.* [1989] found that wave heights were typically well-described by the Rayleigh distribution, but also that departures from Rayleigh occurred for the highest waves in their data set. The Beta-Rayleigh distribution was introduced by *Hughes and Borgman* [1987] to accommodate the high-amplitude cutoff due to depth-limited breaking, and has the form

$$P(\tilde{u}_o) = \frac{2\Gamma(\alpha+\beta)}{\Gamma(\alpha)\Gamma(\beta)} \frac{\tilde{u}_o^{2\alpha-1}}{\tilde{u}^{2\alpha}_{o_{max}}} \left(1 - \frac{\tilde{u}_o^2}{\tilde{u}^2_{o_{max}}}\right)^{\beta-1} \tag{26}$$

valid in the range $0 < \tilde{u}_o < \tilde{u}_{o_{max}}$, where $\tilde{u}_{o_{max}}$ is the depth-limited maximum amplitude, and Γ is the Gamma function. The parameters α and β are given by

$$\alpha = \frac{K_1(K_2 - K_1)}{K_1^2 - K_2}, \tag{27}$$

and

$$\beta = \frac{(1 - K_1)(K_2 - K_1)}{K_1^2 - K_2}, \tag{28}$$

where K_1 and K_2 are related to the RMS and RMQ (root-mean-quad) wave orbital velocity amplitudes by

$$K_1 = \tilde{u}^2_{o_{rms}} / \tilde{u}^2_{o_{max}} \tag{29}$$

and

$$K_2 = \tilde{u}^2_{o_{rmq}} / \tilde{u}^4_{o_{max}}. \tag{30}$$

[67] Figure 15 presents the distributions of $\tilde{u}_{ox}$ for the four energy intervals, together with best fit curves for the Rayleigh and Beta-Rayleigh distributions. (The distributions were determined from the cross-shore component only, as denoted by the subscript x.) The Beta-Rayleigh distribution provides a much better fit to the data, and the departures from Rayleigh increase with increasing wave energy. Thus these distributions indicate that the waves at frame B were increasingly depth-limited as run-averaged wave energies increased.

[68] The values of α, β and $\tilde{u}_{ox_{max}}$ obtained from the fits are listed in Table 6, and were used to determine $\tilde{u}_{ox_{1/3}}$ from equation (26). The $\tilde{u}_{ox_{1/3}}$ estimates are also listed in Table 6, together with the ratio of $\tilde{u}_{ox_{1/3}}$ to $\tilde{u}_{x_{rms}}$. The values of this ratio are very close to 2 for all four intervals. Thus despite the clear departures from Rayleigh in Figure 15, $\tilde{u}_{1/3} = 2\tilde{u}_{rms}$ still holds to a good approximation for the present data set (with the possible exception of Interval IV, given the relatively poor Beta-Rayleigh fit for this interval).

4.7. Breaking Waves

[69] The orbital velocity amplitude distributions in the previous section demonstrate that the waves were increasingly depth-limited through wave energy intervals I to IV, indicating that wave breaking was dynamically important, especially at higher energies. Furthermore, given equation (11), the tendency of the f_w and $\hat{f}_w$ points in Figures 13 and 14 to rise more steeply than the Tolman curve for $\theta_d \gtrsim 1$ indicates higher-than-expected levels of turbulence. Surface-injected turbulence associated with local wave breaking represents one possible source of such additional energy.

[70] Figure 16 shows $\hat{f}_w$ versus θ_d, but with different symbols representing different ranges of the wave breaking frequency at frame B. The wave breaking frequencies were supplied by T. Lippmann, and were obtained using the sub-aerial video techniques described in *Lippmann and Holman* [1991]. Because the video data were limited to daylight hours, wave breaking frequencies are available for only 57 of the 89 of the selected runs. Focusing attention on the region near $\theta_d \sim 1.2$, it is nevertheless seen that there is very little relation between higher values of $\hat{f}_w$ and increased wave breaking frequency. If anything, in fact, there is an inverse

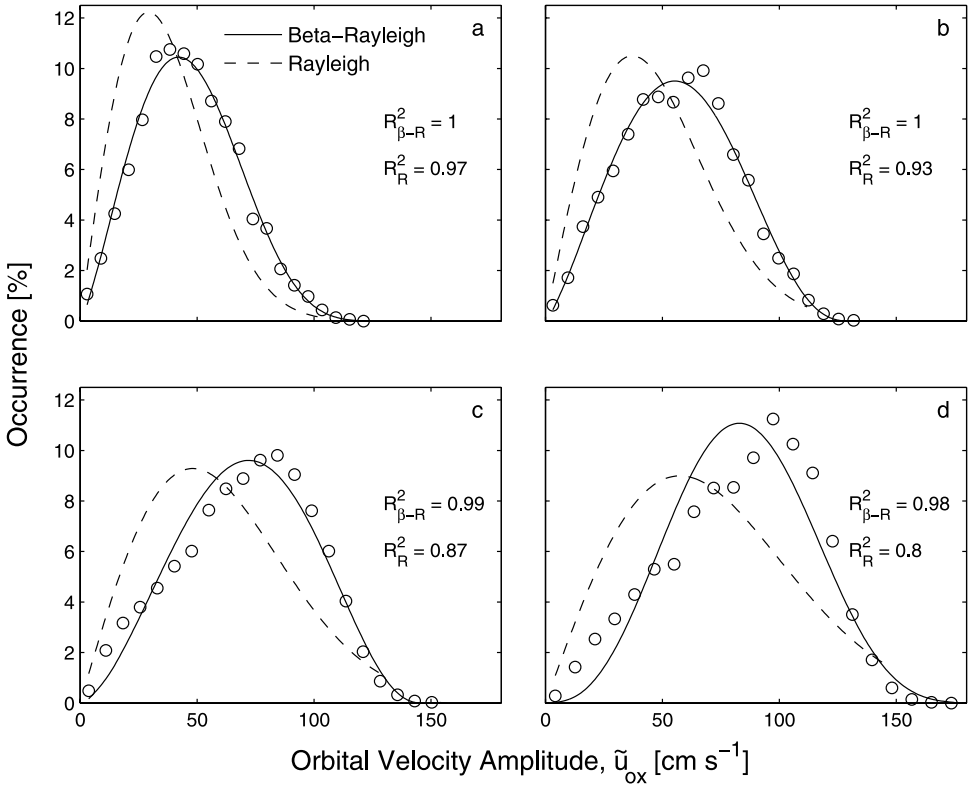

Figure 15. Distributions of wave orbital velocity amplitude for all waves, with fitted Rayleigh and Beta-Rayleigh distributions, for the four energy intervals. Panels (a) through (d) correspond to the increasing ensemble-averaged wave velocities of Intervals I through IV defined in Table 1. Goodness-of-fit is indicated by coefficients of determination for the Rayleigh (R^2_R) and Beta-Rayleigh ($R^2_{\beta\text{-}R}$) distributions from quantile-quantile plots. Numbers of points on which distributions for all waves and for the highest-1/3 waves are based are: (a) 4307, 1428; (b) 3854, 1280; (c) 3692, 1222; (d) 3513, 1164.

relationship between the two quantities. Thus these results indicate that wave breaking was not a likely source of higher near-bed turbulence levels at or near the instrument frame.

[71] While there are no wave breaking frequency estimates at high values of θ_d (i.e., for all but the lowest energy run in Interval IV, for which the wave breaking frequency was 0), the phase-averaged turbulence intensities in Figure 9a support the argument that breaking waves were not the primary source of the additional turbulence at higher wave energies. That is, the facts that the peak turbulence intensities were highest and occurred earliest in the bin nearest the bed points to a near-bed source for the turbulence, not a near-surface source.

4.8. The Δf_w Anomaly, and Other Sources of Additional Turbulent Kinetic Energy

[72] There are a number of possible sources of additional near-bed turbulence to consider other than breaking waves: e.g., wave non-linearity, mean currents, and infragravity waves. In order to explore the different possibilities quantitatively, Δf_w differences were computed between the Tolman curve and the observed f_w values (with $\Lambda = 1.7$). These differences are presented in Figure 17a.

[73] Correlations were computed between the different forcing parameters and Δf_w and $\Delta \hat{f}_w$ for those runs with $\theta_d \geq 0.8$ (61 of the 89-run total). The value of 0.8 corresponds to the flat bed transition: i.e., flat bed occurs at $\theta_{2.5} \sim 1$ [*Nielsen*, 1992], and θ_d is ca. 20% less than $\theta_{2.5}$ (Table 1). The results (Table 7) indicate very weak correlations ($R^2 \lesssim 0.1$) with wave skewness and the mean long-shore current. In contrast, the correlations are comparatively high between both Δf_w and $\Delta \hat{f}_w$ and the RMS sea-and-swell velocity, $\tilde{u}_{rms}$, the mean cross-shore current, $\bar{u}$, and the RMS infragravity wave velocity, $\tilde{U}_{rms}$. The results for wave asymmetry, $As_{\tilde{u}}$, and the significant orbital semi-excursion, $A_{1/3}$, are ambiguous, being either moderately high for Δf_w and low for $\Delta \hat{f}_w$, or the reverse.

[74] The relatively high correlations between $\tilde{u}_{rms}$ and both the f_w and $\hat{f}_w$ anomalies are to be expected, given Figure 17a and the dependence of θ_d on $\tilde{u}_{rms}$. The comparably high values of R^2 for the RMS infragravity wave velocity and the mean cross-shore current are perhaps less

Table 6. Parameters From Best Fits of $\tilde{u}_{ox}$ to the Beta-Rayleigh Distribution[a]

Interval	α	β	$\tilde{u}_{ox_{max}}$, m s^{-1}	$\tilde{u}_{ox_{1/3}}$, m s^{-1}	$\tilde{u}_{ox_{1/3}}/\tilde{u}_{x_{rms}}$	$\tilde{U}_{ox_{1/3}}/\tilde{U}_{x_{rms}}$
I	1.14	7.31	1.39	0.70	2.08	2.00
II	1.33	6.76	1.51	0.82	2.08	1.92
III	1.53	6.35	1.73	1.00	2.06	1.86
IV	1.81	7.29	1.99	1.16	2.04	1.84

[a] Also shown are the maximum values of $\tilde{u}_{ox}$, $\tilde{u}_{ox_{1/3}}$, the ratio $\tilde{u}_{ox_{1/3}}/\tilde{u}_{x_{rms}}$, and the corresponding ratio for infragravity waves. The x subscript indicates that these quantities were determined from the cross-shore component only.

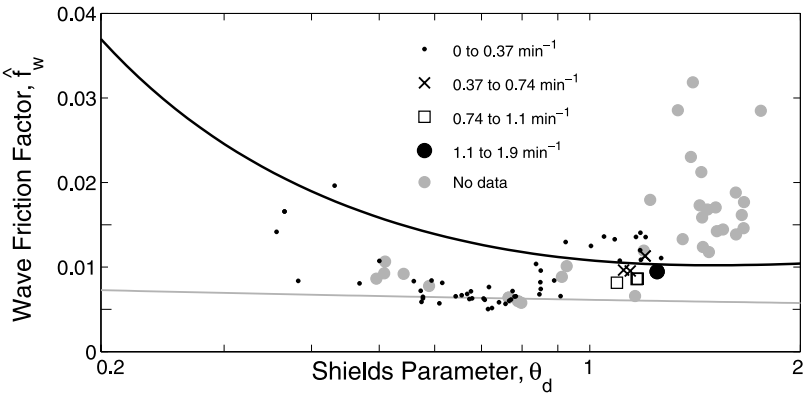

Figure 16. Wave breaking frequency and $\hat{f}_w$. Black symbols indicate the run-mean wave breaking frequency ranges; solid gray circles indicate runs for which wave breaking frequencies were unavailable. $\Lambda = 1.3$. Wave breaking frequencies courtesy of T. Lippmann.

than expected. (Note that, as with $\tilde{u}_{rms}$, $\tilde{U}_{rms}$ is defined to be the square-root of the sum of the u and v variances in the infragravity band). Δf_w is plotted versus infragravity velocity in Figure 17b. The data clearly indicate a relationship between the two quantities for $\theta_d \geq 0.8$. Similarly, there is a comparably strong relationship between Δf_w and the mean cross-shore current (Figure 17c). Thus these results suggest that infragravity waves and the mean cross-shore current (undertow) were potential contributors to the increased turbulence levels in Intervals III and IV.

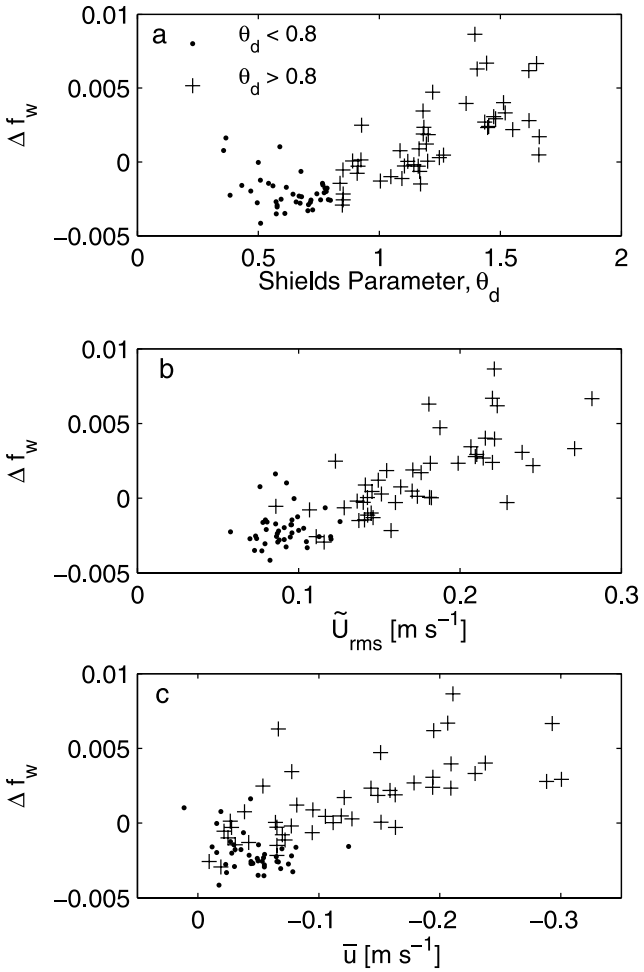

Figure 17. Δf_w versus: (a) Shields parameter; (b) RMS infragravity band velocity, $\tilde{U}_{rms}$; and (c) mean cross-shore velocity, $\bar{u}$. The solid points (•) represent values for $\theta_d \leq 0.8$; the plus signs (+) $\theta_d > 0.8$.

[75] The cross-correlation matrix for the forcing variables in Table 7 is presented in Table 8. The three forcing parameters most correlated with Δf_w and $\Delta \hat{f}_w$ ($\tilde{u}_{rms}$, $\tilde{U}_{rms}$, and $-\bar{u}$) are also correlated with each other. Previous studies have also shown that infragravity and sea-and-swell energies are correlated [*Elgar et al.*, 1992; *Howd et al.*, 1991], so the moderately high cross-correlation between $\tilde{U}_{rms}$ and $\tilde{u}_{rms}$ is expected. The equally high cross-correlation between $\tilde{U}_{rms}$ and $-\bar{u}$ is interesting.

5. Discussion

5.1. The Numerical Value of Λ

[76] Phase-averaging the velocity signal for the purpose of removing the wave orbital motion to obtain time series of turbulent velocity is not a straightforward option for irregular waves. Thus some other velocity-partitioning technique is needed, and the high-pass filter method is a practical choice. As stated previously, the **Λ** correction (equation (21)) arises because the filter method excludes any turbulent energy within the sea-and-swell band from the turbulence intensity estimates.

[77] Ensemble-averaged velocity spectra determined from the ADV records for the four energy intervals are shown in Figure 18. In the sea-and-swell band, the spectral densities

Table 7. Coefficients of Determination, R^2, for Correlations Between the Forcing Parameters Listed and Δf_w for $\theta_d > 0.8$. R^2 Values for $\Delta \hat{f}_w$ are Also Listed

Parameter	R^2 (Δf_w)	R^2 ($\Delta \hat{f}_w$)
$\tilde{u}_{rms}$	0.42	0.63
$\tilde{U}_{rms}$	0.43	0.60
$A_{1/3}$	0.02	0.33
$Sk_{\tilde{u}}$	0.01	0.10
$As_{\tilde{u}}$	0.28	0.03
$-\bar{u}$	0.50	0.42
$\bar{v}$	0.05	0.03

Table 8. Cross-Correlation Matrix Among the Forcing Parameters[a]

	$\tilde{u}_{rms}$	$\tilde{U}_{rms}$	$A_{1/3}$	$Sk_{\tilde{u}}$	$As_{\tilde{u}}$	$-\bar{u}$	$\bar{v}$
$\tilde{u}_{rms}$	1.00	0.79	0.61	0.03	0.02	0.58	0.02
$\tilde{U}_{rms}$		1.00	0.57	0.15	0.01	0.63	0.00
$A_{1/3}$			1.00	0.13	0.01	0.24	0.00
$Sk_{\tilde{u}}$				1.00	0.15	0.00	0.15
$As_{\tilde{u}}$					1.00	0.12	0.06
$-\bar{u}$						1.00	0.01
$\bar{v}$							1.00

[a] R^2 values are listed.

fall off at slopes close to -3 for frequencies immediately above the spectral peak as expected for shallow-water waves [*Kitaigorodskii et al.*, 1975; *Thornton*, 1977], and for higher frequencies at the -5 slope expected for deep-water waves [*Phillips*, 1966]. The spectral slope is steeper still at even higher frequencies, and consequently there is a sharp break in slope where the wave energy spectrum crosses the inertial subrange near 0.6 Hz.

[78] Turbulence production occurs at frequencies in the vicinity of the sea-and-swell peak, and it is expected that the inertial subrange should extend from the production peak to higher frequencies [e.g., *Tennekes and Lumley*, 1972]. By extrapolating the -5/3 line in Figure 18 to 0.1 Hz, one can approximate the contribution to the total turbulence energy from the sea-and-swell band, hence Λ (equation (21)). Figure 18 might indicate that 0.6 Hz would be a more appropriate value for f_c than our chosen value of 0.5 Hz. However, the spectra in this figure are from the ADV, and thus correspond to a measurement point nominally 60 cm above the bed (see section 3). Because the vertical component of high-frequency wave orbital motion decreases rapidly as the bed is approached, the contribution to S_{ww} from irrotational flow in the neighborhood of 0.5 Hz is reduced to negligible levels [*Smyth and Hay*, 2003]. This was the basis for choosing $f_c = 0.5$ Hz, resulting in the range of Λ values used here. Finally, note that the reverse problem, contamination of the turbulence signal by wave motions at frequencies above the cutoff, is much less important because the spectral slope of the wave contribution is much steeper than -5/3, as illustrated by Figure 18 and even more clearly by the pressure and velocity spectra in *Trowbridge and Agrawal* [1995] (their Figure 4).

5.2. Infragravity Wave Turbulence vs. Mean Flow Turbulence

[79] Infragravity waves were identified in section 4 as a possible source of the additional turbulence leading to increased values of Δf_w at higher wave energies (Figure 17). Here, and in section 5.3 and section 5.4 below, support is presented for this result on physical grounds.

[80] The ratios of mean current speed to significant wave orbital velocity were ca. 0.3 or less for all runs (Table 2). Since stress depends on velocity-squared, the usual argument for combined wave-current flows in the weak current case applies: that is, within the thin wave boundary layer, the vertical turbulent momentum flux due to waves dominates the flux due to the mean current [*Grant and Madsen*, 1986; *Fredsoe and Deigaard*, 1992; *Soulsby et al.*, 1993], and the drag coefficient c_D for the mean flow would be increased above the canonical 3×10^{-3} value by about 25% via wave-current interaction (Tables 1 and 2, *Soulsby et al.* [1993]; *Malarkey and Davies* [1998]). With $c_D \sim 4 \times 10^{-3}$ and $f_w \sim 0.01$ (Figure 13), $c_D \sim f_w/2$, and the ratio of current stress to wave stress would be $\sim (\bar{u}^2 + \bar{v}^2)/\tilde{u}_{1/3}^2$ which, using the interval-averaged values in Table 2, would have been about 0.04 on average for all four energy intervals.

[81] The maximum RMS infragravity wave speed approached 0.3 m s^{-1}, which is comparable to maximum mean current speed (Table 2). When multiplied by a factor of 2 to obtain a "significant" amplitude (see Table 6), the interval-averaged infragravity velocities were roughly twice the mean current speeds. Assuming that the friction factors for infragravity and wind waves are similar (see section 5.4), the infragravity stress would have been several times greater than the mean current stress.

5.3. Infragravity Wave Energy and f_w vs. the Mobility Parameter

[82] The spectra in Figure 18 illustrate the increase in infragravity wave energy from Interval I to IV. The infragravity wave part of the spectrum is broad, with a small but significant peak at about 40-s period. We want to examine the possible effect of infragravity wave energy on the concave-upward shape of the f_w versus θ_d plot in Figure 13. However, the grain-roughness Shields parameter depends upon the excursion amplitude, which is ill-defined for this combined flow. Instead, the mobility parameter, $\Psi = 2\theta_d/f_w'$, is used as a non-dimensional energy scale since it is independent of the orbital excursion. Ψ was computed with infragravity wave variances included in the RMS horizontal velocity, giving

$$\Psi = \frac{4\left[\sigma_{\tilde{u}}^2 + \sigma_{\tilde{v}}^2 + \sigma_{IG}^2\right]}{(s-1)g d_{50}}, \tag{31}$$

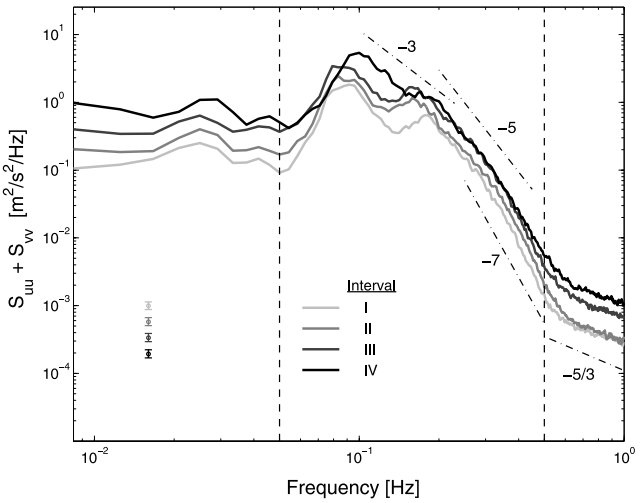

Figure 18. Ensemble-averaged velocity spectra for the four energy intervals, determined from the ADV horizontal velocity data. The spectral levels represent the sum of the u and v power spectral densities. The error bars indicate the 95% confidence limits, based on 480, 421, 404, and 419 degrees of freedom for Intervals 1 through IV, respectively. Vertical dashed lines indicate the upper and lower bounds of the sea-and-swell band. Dash-dot lines indicate different spectral slopes (see text).

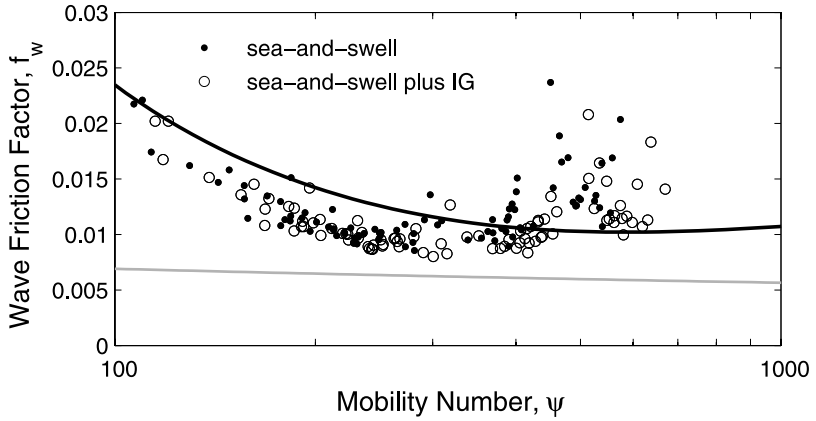

Figure 19. f_w adjusted for infragravity wave energy versus mobility number: for sea-and-swell band energy only (●); and for sea-and-swell plus infragravity energy (○). Λ =1.7. The curves are as in Figure 13.

where σ_{IG}^2 is the total (u and v) variance in the infragravity band.

[83] Assume the turbulence generated by infragravity waves to be statistically independent of that produced by the sea and swell, allowing w'_{rms} to be written as $[w'^2_W + w'^2_{IG}]^{1/2}$, where w'^2_W and w'^2_{IG} are the vertical turbulence intensities due to the sea-and-swell and infragravity waves, respectively. Assume also that the bed stresses due to sea-and-swell and infragravity waves are additive, then $u_*^2 = [\bar{\tau}_W + \bar{\tau}_{IG}]/\rho$, where the overbars denote a time average. Assuming equal friction factors for infragravity and sea-and-swell waves (see section 5.4), equation (19) becomes

$$f_w = 2\frac{(2\Lambda\overline{w'_{rms}})^2}{[\sigma_{\tilde{u}}^2 + \sigma_{\tilde{v}}^2 + \sigma_{IG}^2]}. \tag{32}$$

[84] These results are plotted in Figure 19, together with the model curves. Due to the lack of a suitable estimate of $A_{1/3}$ for combined infragravity and sea-and-swell motions, the model curves are necessarily based on the sea-and-swell parameters only, and are included to provide a convenient visual reference. Two sets of data points are shown: one for f_w and Ψ computed with the RMS horizontal velocity based on the sea-and-swell band variance only (●), and one using the combined sea-and-swell and infragravity band variance (○). The net effect of the infragravity "correction" is to reduce the concave-upward curvature of f_w at the higher θ_d values by: (a) clockwise rotation of the points via the denominator in equation (32); and (b) stretching in the direction of higher θ_d via the numerator in equation (31).

5.4. The Bottom Drag Coefficient for Infragravity Waves

[85] The appropriate value, or range of values, for the bottom drag coefficient for infragravity waves in the near-shore zone is not well known. *Ngusaru and Hay* [2004] obtained improved fits between the observed cross-shore migration rates of lunate megaripples during Duck94 and those predicted from stress-based sediment transport formulae when the bottom friction factor for infragravity waves was equal to that for the sea-and-swell waves (i.e., f_w = 0.02 to 0.05) as opposed to when a current-like value was used. *Henderson and Bowen* [2002] estimated the bottom drag coefficient for infragravity waves using dissipation rates determined from the cross-shore variations in velocity and surface elevation during SandyDuck97, obtaining a value of 0.08. More recently *Henderson et al.* [2006] concluded that non-linear energy transfers were primarily responsible for the observed cross-shore gradients in the infragravity wave energy flux during Duck94. Including dissipation by bottom friction in the energy balance led them to conclude that the infragravity wave drag coefficient had to be less than $O(0.01)$.

[86] *Henderson and Bowen* [2002] and *Henderson et al.* [2006] wrote the instantaneous infragravity wave bottom stress as

$$\tau_{IG}/\rho = C_D\tilde{u}_{rms}\tilde{U}(t). \tag{33}$$

Equation (33) is analogous to the *Longuet-Higgins* [1970] expression for the mean stress in the weak current case [see also *Feddersen et al.*, 1998], but with the mean current replaced by the (slowly varying) infragravity wave velocity. Similarly, one might re-write the expression for the mean stress derived by *Fredsoe and Deigaard* [1992] for weak currents co-linear with sinusoidal waves as

$$\tau_{IG}/\rho = (2\sqrt{2}f_w/\pi)\tilde{u}_{rms}\tilde{U}(t), \tag{34}$$

again replacing the mean current by the infragravity wave velocity. Equations (33) and (34) have the same functional dependence on $\tilde{u}_{rms}$ and $\tilde{U}(t)$. A comparison of the coefficients suggests that the value of C_D could be both proportional to and comparable in magnitude to f_w.

[87] Since contributions made to w'^2 by the horizontal flow are independent of its direction, the quantity of interest here is the time-averaged magnitude of the stress. Using equations (33) and (34), the x and y components of the total stress averaged over a wind-wave cycle are

$$\tau_x/\rho = bf_w\tilde{u}_o\tilde{u}_{ox}(t_s) + C_D\tilde{u}_{rms}\tilde{U}(t_s), \tag{35}$$

and

$$\tau_y/\rho = bf_w\tilde{u}_o\tilde{u}_{oy}(t_s) + C_D\tilde{u}_{rms}\tilde{V}(t_s), \tag{36}$$

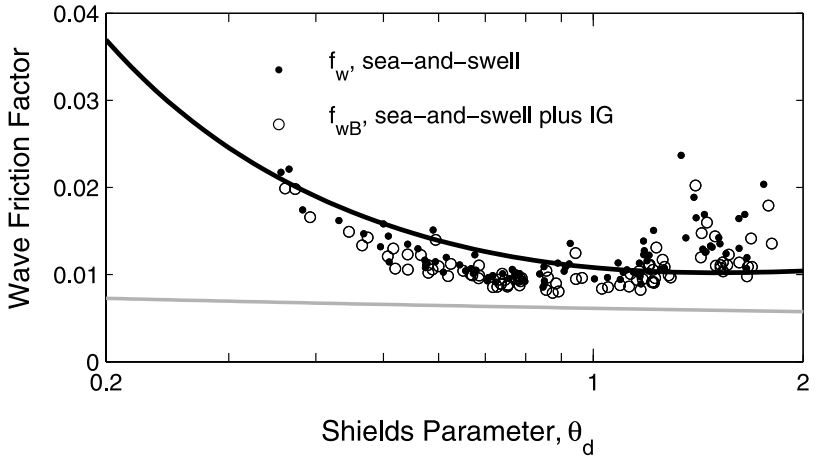

Figure 20. f_w corrected for infragravity wave energy using the best fit value of B from equation (40).

where t_s is the slow timescale of the infragravity wave motions, and it has been assumed that the sea-and-swell stress is dominated by the one peak per wave cycle indicated by the results in section 4.3. The constant factor b arises from the requirement that in the absence of infragravity waves these equations, combined and averaged over time, must yield $\overline{u_*^2} = f_w\tilde{u}_{1/3}^2/2$. For Rayleigh-distributed wave amplitudes, b is very close to unity (equaling 1.002), since $\tilde{u}_{1/3} \sim \sqrt{2}\tilde{u}_{o_{rms}}$. As shown below, however, b drops out of the analysis, so neither its numerical value nor the assumption of Rayleigh statistics are of essential importance here.

[88] The magnitude of the stress becomes

$$u_*^2 = bf_w\tilde{u}_o^2\left\{1 + 2\frac{C_D\tilde{u}_{rms}}{bf_w\tilde{u}_o^3}(\tilde{u}_{ox}\tilde{U} + \tilde{u}_{oy}\tilde{V}) + \left[\frac{C_D\tilde{u}_{rms}}{bf_w\tilde{u}_o^2}\right]^2(\tilde{U}^2 + \tilde{V}^2)\right\}^{1/2}. \quad (37)$$

Since the wave orbital velocity amplitudes are larger than the infragravity wave velocities, and c_D and f_w are assumed to be of the same order, the right-hand side can be expanded in a Taylor series. If it is further assumed that the sea-and-swell orbital velocity amplitudes and the infragravity wave velocities are uncorrelated on average, then the contribution from the cross-terms can be neglected and the time-averaged magnitude of the stress becomes

$$\overline{u_*^2} = \frac{f_w}{2}\tilde{u}_{1/3}^2 + \frac{C_D^2\tilde{u}_{rms}^2}{2f_w\tilde{u}_{1/3}^2}\tilde{U}_{rms}^2. \quad (38)$$

[89] The above equation provides a basis for correcting the estimates of f_w for the effects of infragravity wave turbulence, and simultaneously estimating best fit values of C_D. Since it seems unlikely that C_D would be constant over the range of conditions here, and given the discussion above comparing equations (33) and (34), the assumption is made that C_D is proportional to f_w. Hence

$$C_D = \sqrt{B}f_w, \quad (39)$$

and

$$f_{wB} = f_w\left[1 + \frac{B}{4}\frac{\tilde{U}_{rms}^2}{\tilde{u}_{rms}^2}\right]^{-1}, \quad (40)$$

where f_w is given by equation (19). This equation was used to obtain a least squares fit between f_{wB} and the Tolman-predicted values of f_w with B as the adjustable parameter. Figure 20 shows the resulting values of f_{wB} which, similar to the mobility parameter approach in Figure 19, are less concave upward and exhibit improved agreement with the prediction based on the Wilson sheet-flow roughness model. The best fit value of B is 4.91, yielding $C_D = 2.2f_w$. Thus the turbulence data indicate that the drag coefficient for infragravity waves is the same order as the wave friction factor.

5.5. Sheet Flow Roughness

[90] The above analysis indicates that the faster rate of increase of f_w with θ_d is at least partly attributable to increased near-bed turbulence levels associated with infragravity waves. The infragravity correction to f_w is significant, amounting to 10–20% at the higher values of the Shields parameter, and leads to improved agreement with predictions based on Wilson's parameterization for sheet flow roughness. Thus the present results appear to support equation (6), or at least do not contradict it. Given that Wilson's expression is based on unidirectional flow data, this level of agreement with measurements made in the field and in irregular waves is rather encouraging.

5.6. Speculative Remarks

[91] High suspended sediment concentration gradients in the WBL are expected to damp out turbulence [*Glenn and Grant*, 1987]. One might therefore expect lower levels of turbulence near a mobile bed than a bed of fixed grains. The peak near-bed concentrations observed here were $O(10)$ kg/m^3 or less (e.g., Figure 7), which is not very high (less than 0.5% by volume). The effects of turbulence damping by sediment stratification have not been taken into consideration but might contribute to the observed values of f_w falling below the Tolman curve at small and intermediate values of the Shields parameter.

[92] For sufficiently high values of the horizontal pressure gradient, the bed sediments may move as a plug [*Madsen*, 1974; *Sleath*, 1999], and changes in the magnitude and wave phase of peak turbulence would be expected [*Zala Flores and Sleath*, 1998]. Sleath introduced the parameter S, the ratio of the horizontal pressure gradient force to the buoyancy force acting on a sediment grain. At a given instant of time, S is

$$S(t) = \frac{d\tilde{u}/dt}{(s-1)g}. \tag{41}$$

[93] Peak values, $\hat{S}$, were determined from the maximum value of $S(t)$ for each wave in the selected runs [*Newgard*, 2004]. The maxima of the $\hat{S}$ distributions had values of 0.04, 0.05, 0.07 and 0.08 for Intervals I through IV, respectively. The highest value of $\hat{S}$ for all waves in the 89 runs was 0.14. According to *Sleath* [1994, 1999], S should exceed 0.3 for plug flow to occur in flat beds of uncompacted sand. The observed values of $\hat{S}$ therefore indicate that plug flow was unlikely.

[94] Finally, the present results exhibit an abrupt change toward higher turbulence intensities at a wave Reynolds number near 1.2×10^6 (Figure 10); this change is also reflected in the shift to higher values of $\hat{f}_w$ at $\theta_d \sim 0.8$ in Figure 14. Since the infragravity wave correction does not completely account for the discrepancy between the observed and predicted trends of f_w at high wave energies, a critical wave Reynolds number leading to higher than expected turbulence intensities is an interesting possibility.

6. Summary and Conclusions

[95] Results have been presented for turbulence intensity and bottom friction in the near-shore wave bottom boundary layer over a mobile sandy bed during high-energy wave conditions. The incident sea-and-swell waves during the 89 selected data runs were characterized by 50- to 130-cm s^{-1} significant wave orbital velocities, 10-s to 11-s peak periods, and wave Reynolds numbers from 5×10^5 to 3×10^6. Wave non-linearity was moderate to high, with skewnesses ranging from 0.25 to 1.15 and asymmetries from -0.15 to +0.37 (the positive sign indicating waves pitched forward in time, and thus backward in space). Grain roughness Shields parameters ($\theta_{2.5}$) ranged from 0.4 to 2, indicating that the data span the range of bed states from low steepness anorbital ripples to flat bed, and extend well into the sheet flow regime. The long-shore current was 12 cm s^{-1} on average, ranging from 1 to 21 cm s^{-1}. The mean cross-shore current was offshore for most runs, and -10 cm s^{-1} on average, ranging from -30 to 1 cm s^{-1}. Mean current speed to significant wave orbital velocity ratios were 0.19 on average with a 0.04 to 0.31 range, so wave stress was the dominant bottom friction term. RMS infragravity wave velocities ranged from 6 cm s^{-1} to 28 cm s^{-1}.

[96] Near-bed RMS vertical turbulent velocities were 1 to 4 cm s^{-1}, with peak values occasionally reaching $O(10)$ cm s^{-1}. Wave-phase averages of the turbulence intensity over the highest-1/3 waves in each run demonstrate that the turbulence typically peaked once per wave cycle, and that this peak typically occurred close to the wave crest. For $\theta_{2.5} > 1.5$ (i.e., full sheet flow conditions), the turbulence peak was largely confined to range bins within 2 to 3 cm of the bed, occurring at a phase of 15° in the range bin nearest the bed and at progressively later phases and reduced amplitudes at greater heights. These variations with height are qualitatively consistent with diffusive growth of the wave bottom boundary layer. In the bin nearest the bed, the amplitude (phase) of peak turbulence intensity increased (decreased) with increasing wave Reynolds number. The turbulence generated under the wave crest decayed to near background levels prior to the following trough, indicating that there can have been little if any memory of the crest-generated turbulence from one wave to the next. Typically, one primary turbulence intensity peak occurred per wave cycle, consistent with the high values of wave orbital velocity skewness.

[97] A central result of this study is the favorable agreement between the observed estimates of the wave friction factor, f_w, and the values predicted using Tolman's version of the WBL relations, these being based in part on the expressions introduced by *Madsen et al.* [1990] for ripple roughness under irregular waves and by *Wilson* [1989] for sheet flow roughness in oscillatory flow. Given that our observed values of f_w derive from a simple, (mainly) laboratory-based relation between friction velocity and near-bed vertical turbulence intensity, and that the model predictions are based on laboratory measurements of sheet flow roughness in unidirectional flow, this agreement between model-predicted and field-measured values of f_w is rather remarkable.

[98] Two corrections to the values of u_* obtained from the near-bed vertical turbulence intensities are implemented. One, denoted here by the parameter Λ, is an approximate correction to account for the turbulence energy contained within the sea-and-swell band. The second correction is an adjustment for the additional turbulence energy production due to motions outside the sea-and-swell band. The occurrence of this additional energy is indicated in the results by: (a) amplification of the high-amplitude tail in the probability distribution for the turbulence intensity with increasing wave energy; and (b) a rate of increase of f_w with θ_d at the upper end of the observed Shields parameter range that is anomalously high compared to that predicted by Wilson's sheet flow model.

[99] The anomalous departure from Wilson's model is correlated with RMS infragravity wave energy and with the mean cross-shore current speed, but not with other forcing parameters distinct from θ_d: that is, not with the mean long-shore current, nor with wave skewness or asymmetry. Thus wave non-linearity is not a likely source for the additional turbulence. The mean cross-shore current is highly correlated with the infragravity wave energy, and is also a possible source of the additional turbulence. However, the stress due to infragravity waves is estimated to be several times larger than that associated with the mean flow. Approximate but plausible corrections for infragravity wave energy significantly reduce the discrepancy between the Wilson model predictions and the observed friction factors. Thus we conclude on physical grounds that infragravity waves are a likely source for the additional turbulence.

[100] The Beta-Rayleigh distribution fits to the wave orbital velocity amplitudes indicate that the waves were depth-limited by breaking for the higher wave energy runs.

The wave breaking frequency data, however, do not indicate a relationship between increased f_w (i.e., increased near-bed turbulence) and higher frequencies of breaker occurrence at the instrument frame location. Partly on this basis, and partly because the vertical variation of the wave-phase averaged turbulence for the highest-1/3 waves clearly indicates that the bed is the primary source of turbulence in the several cm immediately adjacent to the bottom, we conclude that turbulence generated at the sea surface by breaking waves did not have significant influence on the results.

[101] One of the questions at the outset of this study was whether values of f_w based on the properties of the equivalent "significant" wave would be comparable to values based on the peak turbulence intensities for the highest-1/3 waves in each run, $\hat{f}_w$. This question has been answered in the affirmative, but there is a caveat. That is, while the values of f_w and $\hat{f}_w$ are essentially the same for $\theta_d < 0.8$, at higher values of the Shields parameter $\hat{f}_w$ is proportional to but larger than f_w. This difference at high Shields parameters parallels the departure of f_w from the Wilson model and is also reflected in the progressive growth with wave energy of the high-amplitude tail of the vertical turbulent velocity probability distribution functions. One possible inference is that, at high wave energies, non-linear interaction between waves in the infragravity and sea-and-swell bands may contribute significantly to peak near-bed turbulence.

[102] The observed variations of peak turbulence intensity with wave phase are reasonably consistent with previously reported results from laboratory experiments and numerical simulations at comparable wave Reynolds numbers, both in terms of the absolute value of the wave phase at which the ensemble-averaged peak turbulence occurs, and the wave Reynolds number dependence of this phase. However, the laboratory and numerical studies cited here were carried out with sinusoidal wave forcing, and the numerical studies have assumed a smooth, fixed bed. A need for numerical simulations with skewed waves and mobile beds is indicated. The peak turbulence intensity observations exhibit an abrupt change near a wave Reynolds number of 1.2×10^6. For $Re \lesssim 1.2 \times 10^6$, peak turbulence intensities were independent of Re, consistent with previous results [*Smyth and Hay*, 2003] indicating that bottom stress for different rippled bed states was independent of wave energy. For $Re \gtrsim 1.2 \times 10^6$, peak turbulence intensities steadily increased. Thus the possibility of a critical value of the wave Reynolds number near 1.2×10^6 is indicated, above which turbulence intensities increase with Re and therefore also with Shields parameter.

[103] In summary, friction velocities and wave friction factors have been determined for high-energy conditions extending into the sheet flow regime, and are found to be in substantial agreement with the predictions of semi-empirical eddy viscosity models of the wave bottom boundary layer as summarized by *Tolman* [1994] and with the formula for sheet flow roughness proposed by *Wilson* [1989] in particular. The agreement between observations and predictions provides a field-based constraint upon the range of f_w values at higher wave energies, and consequently the choice of sheet flow roughness model for field conditions is at least somewhat less "arbitrary" than a decade ago [*Tolman*, 1994]. Because the friction factor estimates are based on an indirect measure of bottom stress, further field measurements using redundant measures of stress are needed. Infragravity waves contributed to near-bed turbulence in high-energy wave conditions, enabling an estimate of the bottom drag coefficient for infragravity waves. The assumptions underpinning this estimate are rather weak, however, and, together with the relatively small number of estimates of C_D in the literature, serve to underscore the present uncertainty in the specification of bottom stress for this part of the forcing spectrum. The observed variation of peak turbulence intensity as a function of wave phase and wave Reynolds number above a (mainly) flat mobile bed under skewed waves should provide a useful basis of comparison with turbulence intensity predictions from the various turbulence-resolving numerical models currently under development. The indication of increased turbulence production at values of Re above 1.2×10^6 merits further investigation.

[104] **Acknowledgments.** The authors wish to thank Bill Birkemeier and the FRF staff for their cooperation and support, without which this research would not have been possible. We also thank Carolyn Smyth for useful discussions related to her research, Len Zedel for his work on the development of the CDP, and Tom Lippman for providing the wave breaking frequencies. We also thank Robert Craig and Wes Paul for their very capable technical support, and the graduate students and other staff members from Dalhousie and Memorial who participated in SandyDuck97. This work was funded by the U.S. Office of Naval Research Coastal Sciences Program and the Natural Sciences and Engineering Research Council of Canada.

References

Ardhuin, F., W. O'Reilly, T. Herbers, and P. F. Jessen (2003), Swell transformation across the continental shelf. Part I: Attenuation and directional broadening, *J. Phys. Oceanogr.*, *33*, 1921–1939.

Batchelor, G. (1953), *The Theory of Homogeneous Turbulence*, Cambridge Univ. Press, New York.

Birkemeier, W. A., H. C. Miller, S. D. Wilhelm, A. E. DeWall, and C. S. Gorbics (1985), A user's guide to the Coastal Engineering Center's (CERC's) Field Research Facility, *Tech. Rep. CERC-85-1*, Coastal Eng. Res. Center, U.S. Army Corps of Eng., 137 p.

Chang, Y. S., and A. Scotti (2006), Turbulent convection of suspended sediments due to flow reversal, *J. Geophys. Res.*, *111*, C07001, doi:10.1029/2005JC003240.

Clay, C. S., and H. Medwin (1977), *Acoustical Oceanography: Principles and Applications*, Wiley, New York, 544 p.

Conley, D. C., and D. L. Inman (1992), Field observations of the fluid–granular boundary layer under near–breaking waves, *J. Geophys. Res.*, *97*, 9631–9643.

Crawford, A. M., and A. E. Hay (2001), Linear transition ripple migration and wave orbital velocity skewness: Observations, *J. Geophys. Res.*, *106*, 14,113–14,128.

Dingler, J. R., and D. L. Inman (1977), Wave–formed ripples in nearshore sands, in *Proc. 15th Coastal Eng. Conf.*, vol. 2, p. 2109–2126, Am. Soc. of Civ. Eng., New York.

Elgar, S., and R. T. Guza (1985), Observations of bispectra of shoaling surface gravity waves, *J. Fluid Mech.*, *161*, 425–448.

Elgar, S., T. Herbers, M. Okihiro, J. Oltman-Shea, and R. Guza (1992), Observations of infragravity waves, *J. Geophys. Res.*, *97*(C10), 15,573–15,577.

Feddersen, F., R. T. Guza, S. Elgar, and T. H. C. Herbers (1998), Alongshore momentum balances in the nearshore, *J. Geophys. Res.*, *103*, 15,667–15,676.

Foster, D., R. Beach, and R. Holman (2000), Field observations of the wave bottom boundary layer, *J. Geophys. Res.*, *105*, 19,631–19,647.

Fredsoe, J., and R. Deigaard (1992), *Mechanics of Coastal Sediment Transport*, World Sci., 369 p.

Glenn, S. M., and W. D. Grant (1987), A suspended sediment correction for combined wave and current flows, *J. Geophys. Res.*, *92*, 8244–8264.

Grant, W., and O. Madsen (1982), Movable bed roughness in unsteady oscillatory flow, *J. Geophys. Res.*, *87*, 469–481.

Grant, W., and O. Madsen (1986), The continental-shelf bottom boundary layer, *Annu. Rev. Fluid Mech.*, *18*, 265–305.

Guza, R. T., and E. B. Thornton (1980), Local and shoaled comparisons of sea surface elevations, pressures and velocities, *J. Geophys. Res.*, *85*, 1524–1530.

Hay, A. E. (1991), Sound scattering from a particle-laden turbulent jet, *J. Acoust. Soc. Am.*, *90*, 2055–2074.
Hay, A., and T. Mudge (2005), Primary bed states during SandyDuck97: Occurrence, spectral anisotropy, and the bed state storm cycle, *J. Geophys. Res.*, *110*, C03013, doi:10.1029/2004JC002451.
Henderson, S. M., and A. J. Bowen (2002), Observations of surf beat forcing and dissipation, *J. Geophys. Res.*, *107*(C11), 3193, doi:10.1029/2000JC000498.
Henderson, S. M., R. T. Guza, S. Elgar, T. H. C. Herbers, and A. J. Bowen (2006), Nonlinear generation and loss of infragravity wave energy, *J. Geophys. Res.*, *111*, C12007, doi:10.1029/2006JC003539.
Herbers, T. H. C., M. Orzech, S. Elgar, and R. T. Guza (2003), Shoaling transformation of wave frequency-directional spectra, *J. Geophys. Res.*, *10*(C1), 3013, doi:10.1029/2001JC001304.
Howd, P., J. Oltman-Shay, and R. Holman (1991), Wave variance partitioning in the trough of a barred beach, *J. Geophys. Res.*, *96*, 12,781–12,795.
Hughes, S., and L. Borgman (1987), Beta-Rayleigh distribution for shallow water wave heights, in *Coastal Hydrodynamics*, edited by R. Dalrymple, p. 17–31, Am. Soc. Civ. Eng., New York.
Jensen, B., B. Sumer, and J. Fredsoe (1989), Turbulent oscillatory boundary layers at high Reynolds numbers, *J. Fluid Mech.*, *206*, 265–297.
Jonsson, I. (1966), Wave boundary layers and friction factors, in *Proc. 10th Coastal Eng. Conf.*, vol. 1, p. 127–148, Am. Soc. Civ. Eng., New York.
Jonsson, I. (1980), A new approach to oscillatory rough turbulent boundary layers, *Ocean Engng.*, *7*, 109–152.
Kitaigorodskii, S. A., V. P. Krasitskii, and M. M. Zaslavskii (1975), On Phillips' theory of equilibrium range in the spectra of wind-generated waves, *J. Phys. Oceanogr.*, *5*, 410–420.
Kos'yan, R., H. Kunz, S. Kuznetsov, N. Pykhov, and M. Krylenko (1996), Sand suspension events and intermittence of turbulence in the surf zone, in *Proc. 25th Coastal Eng. Conf.*, p. 4111–4119, Am. Soc. Civ. Eng., New York.
Levine, D., P. Ramsey, and R. Smidt (2001), *Applied Statistics for Eng. and Scientists*, Prentice-Hall, New Jersey.
Lippmann, T. C., and R. A. Holman (1991), Phase speed and angle of breaking waves measured with video techniques, in *Coastal Sediments '91*, edited by N. Kraus, p. 542–556, Am. Soc. Civ. Eng., New York.
Longuet-Higgins, M. (1952), On the statistical distribution of the heights of sea waves, *J. Mar. Res.*, *11*(3), 245–266.
Longuet-Higgins, M. (1970), Longshore currents generated by obliquely incident sea waves, 1, *J. Geophys. Res.*, *75*(33), 6778–6789.
Madsen, O. (1974), Stability of a sand bed under breaking waves, in *Proc. 14th Coastal Eng. Conf.*, p. 776–794, Am. Soc. Civ. Eng., New York.
Madsen, O., P. Mathisen, and M. Rosengaus (1990), Movable bed friction factors for spectral waves, in *Proc. 22nd Coastal Eng. Conf.*, p. 420–429, Am. Soc. Civ. Eng., New York.
Malarkey, J., and A. Davies (1998), Modelling wave-current interactions in rough turbulent bottom boundary layers, *Ocean Eng.*, *25*, 119–141.
Newgard, J. P. (2004), Near-bed turbulence and flat bed wave friction factors in the nearshore zone, M.Sc. thesis, Dalhousie Univ., Halifax, Nova Scotia, Canada, 121 p.
Ngusaru, A. S., and A. E. Hay (2004), Cross-shore migration of lunate megaripples during Duck94, *J. Geophys. Res.*, *109*, 16 pp., C02006, doi:10.1029/2002JC001532.
Nielsen, P. (1992), *Coastal Bottom Boundary Layers and Sediment Transport*, World Sci., River Edge, New Jersey, 324 p.
Phillips, O. M. (1966), *The Dynamics of the Upper Ocean*, Cambridge Univ. Press, London, 261 p.
Schlichting, H. (1932), Berechnung über periodischer grenzschichtströmungen, *Phys. Z.*, *33*, 327–335.
Schlichting, H. (1979), *Boundary Layer Theory*, 7th ed., McGraw-Hill Inc., New York.
Sleath, J. (1987), Turbulent oscillatory flow over rough beds, *J. Fluid Mech.*, *182*, 369–409.
Sleath, J. (1994), Bed load transport in oscillatory flow, in *Sediment Transport Mechanisms in Coastal Environments and Rivers*, edited by M. Belorgey, R. Rajaona, and J. Sleath, p. 93–106, World Sci., River Edge, New Jersey.
Sleath, J. (1999), Conditions for plug formation in oscillatory flow, *Cont. Shelf Res.*, *19*, 1643–1664.
Smyth, C., and A. E. Hay (2002), Wave friction factors in nearshore sands, *J. Phys. Oceanogr.*, *32*, 3490–3498.
Smyth, C., and A. Hay (2003), Near-bed turbulence and bottom friction during SandyDuck97, *J. Geophys. Res.*, *108*(C6), 3197, doi:10.1029/2001JC000952, 28–1–28–14.
Smyth, C., A. E. Hay, and L. Zedel (2002), Coherent Doppler profiler measurements of near-bed suspended sediment fluxes and the influence of bedforms, *J. Geophys. Res.*, *107*(C8), 3105, doi:10.1029/2000JC000760, 19–1–19–20.
Soulsby, R. L., L. Hamm, G. Klopman, D. Myrhaug, and G. Thomas (1993), Wave-current interaction within and outside the bottom boundary layer, *Coast. Eng.*, *21*, 41–69.
Spalart, P. R., and B. S. Baldwin (1987), Direct simulation of turbulent oscillatory boundary shear, *Turbulent Shear*, 6.
Swart, D. (1974), Offshore sediment transport and equilibrium beach profiles, *Tech. Rep. 131*, Delft Hydraulics Lab.
Tennekes, H., and J. L. Lumley (1972), *A First Course in Turbulence*, MIT Press, Cambridge, MA, 300 p.
Thornton, E. B. (1977), Rederivation of the saturation range in the frequency spectrum of wind-generated gravity waves, *J. Phys. Oceanogr.*, *7*, 137–140.
Thornton, E. B., and R. T. Guza (1983), Transformation of wave height distribution, *J. Geophys. Res.*, *88*, 5925–5938.
Thornton, E., and R. Guza (1989), Wind wave transformation, in *Nearshore Sediment Transport*, edited by R. Seymour, p. 137–181, Plenum Press, New York.
Tolman, H. (1994), Wind waves and moveable-bed bottom friction, *J. Phys. Oceanogr.*, *24*, 994–1009.
Trowbridge, J., and Y. Agrawal (1995), Glimpses of a wave boundary layer, *J. Geophys. Res.*, *100*(C10), 20,729–20,743.
Trowbridge, J., and O. Madsen (1984), Turbulent wave boundary layers 1. Model formulation and first -order solution, *J. Geophys. Res.*, *89*, 7989–7997.
van Doorn, T. (1981), Experimental investigation of near-bottom velocities in water waves with and without a current, *Tech. Rep. TOW Report M 1423*, Delft Hydraulics Laboratory.
Wilson, K. (1989), Friction of wave-induced sheet flow, *Coastal Eng.*, *12*, 371–379.
Young, I. R., and R. M. Gorman (1995), Measurements of the evolution of ocean wave spectra due to bottom friction, *J. Geophys. Res.*, *100*, 10,987–11,004.
Zala Flores, N., and J. Sleath (1998), Mobile layer in oscillatory sheet flow, *J. Geophys. Res.*, *103*(C6), 12,783–12,793.
Zedel, L., and A. Hay (1999), A coherent Doppler profiler for high resolution particle velocimetry in the ocean: Laboratory measurements of turbulence and particle flux, *J. Atmos. Ocean. Tech.*, *16*(8), 1102–1117.

A. E. Hay and J. P. Newgard, Department of Oceanography, Dalhousie University, Halifax, NS, Canada, B3H 4J1. (alex.hay@phys.ocean.dal.ca)